Physics

SCIENCE OF LIGHT

VOLUME 8 NUMBER 2

December

1959

OHIO STATE UNIVERSITY
NOV 6 - 1961
LIBRARY

Published by the

Institute for Optical Research

Tokyo University of Education

in collaboration with

The Spectroscopical Society of Japan

SCIENCE OF LIGHT

Science of Light contains reports of the Institute for Optical Research and contribution from other science bodies about similar subjects.

The editorial staff consists of following members:

Chairman: Prof. H. Ootsuka, *Tokyo University of Education*

Dr. Y. Fujioka, *Atomic Energy Commission of Japan*

Prof. E. Minami, *Tokyo University*

Prof. M. Seya, *Tokyo University of Education*

Prof. Y. Uchida, *Kyoto University*

Prof. T. Uemura, *Rikkyo University*

Prof. K. Miyake, *Tokyo University of Education*

All communications should be addressed to the director or to the librarian of the Institute.

The Institute for Optical Research

Tokyo University of Education

400, Hyakunin-tyo-4, Sinzyuku-ku, Tokyo, Japan

Printed at
the Printing Department, Chūō Kagakusha,
Tokyo

SCIENCE OF LIGHT VOLUME 8, NUMBER 2, 1959

Theory on Concave Grating Mountings for Photoelectric-Spectrometric Use

Kazuo P. MIYAKE

Institute for Optical Research, Tokyo University of Education
Shinjuku-ku, Tokyo

(Received December 5, 1959)

Abstract

With the concave grating, the conditions for obtaining a good imagery by rotating it around an axis that passes through a suitable point and is parallel to the grating grooves to change the wavelength of diffracted rays are derived from the formula given by Beutler. Only the rays lying in the meridional plane passing the vertex of the grating and normal to the grooves are considered to be the image-forming rays.

A group of mountings that are of good imaging performance and practicable for photoelectric-spectrometric use is found by equating w^2 and w^3 terms of the Beutler's formula simultaneously to zero. The well-known Eagle mounting and Wadsworth mounting belong to this group as special cases.

The formulas for determining the position of the axis of rotation, which gives a good imagery for a range of wavelength with a set direction of emerging rays, are derived.

The condition for eliminating the astigmatism is discussed briefly.

§ 1. Introduction

The concave grating forms images of a slit as spectral lines without the use of any other optical system. This is an excellent feature of the concave grating as an element of spectrometers used for such radiation as the extreme ultraviolet rays for which there exists no transmitting or highly reflecting materials.

In most of the conventional mountings of the concave grating, Rowland circle is being used, for the setup is exclusively in combination with photographing arrangement. Surely the mounting conforming to the Rowland circle has a distinguished advantage; it is preferred especially when a concave grating with considerable width is used.

With recent developments in the photoelectric photometry, the concave grating is apt to be used as an element of spectrometer in combination with photomultiplier. The conditions required for the concave grating to be used in photoelectric-spectrometric work are:

(a) The entrance and exit slits are fixed.
(b) The directions of incident and emergent bundles of rays are kept set.
(c) The displacement of the grating is small and therefore the illuminating rays do not move appreciably over the grating surface.

A new type of mounting fulfilling these conditions was devised and its principle was given by Seya[1]. Greiner and Schäffer made further study on the Seya mounting[2][3]. The principle of this new mounting is that the entrance and exit slits are fixed and the concave grating is rotated around an axis that passes through the vertex of the grating and is parallel to the grooves of the grating whereby the wavelength of emerging rays is changed. By choosing properly the positions of entrance and exit slits at the start, the condition for imagery can be satisfied to the second order with respect to the angle of rotation. Although this mounting allows the directions of principal rays of incident and emergent bundles of rays to be kept unaltered and therefore is quite suited to spectrometric use, the angle between the incident and emergent rays can not be chosen arbitrarily but must be fixed to about 70 degrees. As the result the angles of incidence and diffraction become comparatively large and therefore so is the astigmatism.

As Seya mounting does not conform to the Rowland's condition, the width of grating in his mounting must be reduced to some extent.

Onaka devised a mounting[4] locating the axis of rotation at a point away from the grating vertex. This satisfied the condition for imagery to the first order with respect to the angle of rotation and allowed the angle between incident and emergent rays to be chosen with some degree of freedom. On this principle he constructed a vacuum ultraviolet monochromater. In this mounting, the directions of incident and emergent rays change to some extent. Though it can satisfy the Rowland's condition at a given wavelength, it seems likely that for wider wavelength range its imaging performance becomes inferior to that of Seya mounting.

The author has undertaken a general analysis on the mounting of concave grating suitable for photoelectric-spectrometric use utilizing only the rotation around an axis parallel to the grooves of the grating as the simple mechanism for changing the wavelength. The result of analysis is described below.

§ 2. General Theory

The problems discussed in this paper are concerned with 1) the conditions under which the imagery becomes correct with fixed entrance and exit slits and within

1) M. Seya: Science of Light (Tokyo), **2**, (1951) 8.
2) H. Greiner und E. Schäffer: Optik, **14**, (1957) 263.
3) H. Greiner und E. Schäffer: Optik, **15**, (1958) 51.
4) R. Onaka: Science of Light (Tokyo), **7**, (1958) 23.

some range of angle of rotation of the grating around an axis passing through a suitable point and parallel to the grating grooves, and 2) the optimum position of the axis of rotation.

The imagery of the meridional rays that lie in the plane passing the vertex of the grating and normal to the grooves is considered mainly in the following. The imagery of the sagittal rays is considered only briefly in the latter part of this paper.

Two cases are considered. One is the case in which the cross section of the bundle of incident rays passing through the entrance slit and falling on the grating surface is large compared with the whole area of the concave grating. In this case, the bundle of rays effective for imagery is restricted by the area of the grating and therefore the principal ray of the effective bundle is always incident at the vertex of the grating. This case will be called Case I hereafter. The other is the case in which the area of the grating is large compared with the cross section of the bundle of incident rays or a stop is provided between the grating and the exit (or entrance) slit to have the direction of emergent (or incident) rays fixed and the illuminating rays move over the grating surface. This case will be referred to as Case II. In short, the directions of incident and emergent rays change but the same part of the grating surface is illuminated in Case I, while in Case II, the bundle of either incident or emergent rays is fixed and different parts of the grating surface are illuminated. From the practical point of view, Case II seems to be preferable to Case I, but as the calculation for Case I is easier and this case is also applicable under certain circumstances, Case I is treated first and from its results the calculation for Case II is derived.

The case treated by Onaka is a special case of Case I and in Seya mounting Case I and II become undistinguishable.

Consider the plane which is normal to the grating grooves and passes the grating vertex, and treat the problem hereafter on this plane two-dimensionally..

2.1 Calculation for Case I

In Fig. 1, let

$E(\rho\cos\alpha_0,\ \rho\sin\alpha_0)$: the entrance slit,
$A(\rho'\cos\beta_0,\ \rho'\sin\beta_0)$: the exit slit,
$G(O,\ O)$: the initial position of the grating vertex,
$C(R,\ O)$: the initial position of the centre of curvature of the concave grating,
α_0 : the initial angle of incidence of the principal ray,
β_0 : the initial angle of diffraction of the principal ray,

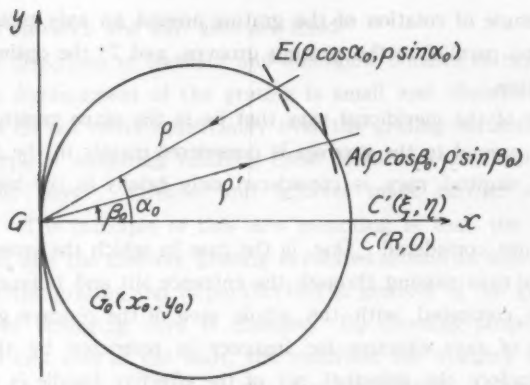

Fig. 1

$\rho=GE$, $\rho'=GA$,

R: the radius of curvature of the concave grating.

The same sign is to be assigned to α_0 and β_0 when both the incident and diffracted rays are on the same side of the normal at the grating vertex.

Let $O(X, Y)$ be the centre of rotation. The optimum values of X and Y will be determined as the result of the following calculation.

If the concave grating is rotated about the point O through an angle ω, the position of the centre of curvature $C'(\xi, \eta)$ is given by the following expressions.

$$\left.\begin{aligned}\xi-X&=(R-X)\cos\omega+Y\sin\omega\\ \eta-Y&=(R-X)\sin\omega-Y\cos\omega\end{aligned}\right\} \tag{1}$$

The position of the grating vertex $G_0(x_0, y_0)$ is given by

$$\left.\begin{aligned}x_0&=(1-\cos\omega)X+Y\sin\omega\\ y_0&=-\sin\omega X+(1-\cos\omega)X\end{aligned}\right\}. \tag{2}$$

The distances r and r' of the entrance and exit slits respectively from G_0 are given by

$$\left.\begin{aligned}r^2&=(\rho\cos\alpha_0-x_0)^2+(\rho\sin\alpha_0-y_0)^2\\ r'^2&=(\rho'\cos\beta_0-x_0)^2+(\rho'\sin\beta_0-y_0)^2\end{aligned}\right\}. \tag{3}$$

The angles α and β of incidence and diffraction respectively of the principal ray falling at G_0 are determined by

$$\left.\begin{aligned}\cos\alpha&=\{(\rho\cos\alpha_0-x_0)(\xi-x_0)+(\rho\sin\alpha_0-y_0)(\eta-y_0)\}/Rr\\ \cos\beta&=\{(\rho'\cos\beta_0-x_0)(\xi-x_0)+(\rho'\sin\beta_0-y_0)(\eta-y_0)\}/Rr'\\ \sin\alpha&=\{(\rho\sin\alpha_0-y_0)(\xi-x_0)-(\rho\cos\alpha_0-x_0)(\eta-y_0)\}/Rr\\ \sin\beta&=\{(\rho'\sin\beta_0-y_0)(\xi-x_0)-(\rho'\cos\beta_0-x_0)(\eta-y_0)\}/Rr'\end{aligned}\right\}. \tag{4}$$

To test the degree of perfection of the imagery attained by a given mounting the expressions given by Beutler[5] are used here with notations as original as possible for the present work to go with his.

At present, the image formed only by the rays lying in the plane passing the grating vertex and normal to the grooves is considered, therefore we put $z=z'=l=0$ in the Beutler's expression. Retaining the terms up to those with the fourth power of w, the Beutler's expression becomes

$$\begin{aligned}
F+F'=&r+r'-w(\sin\alpha+\sin\beta)+m\lambda w/d\\
&+\frac{w^2}{2}\left\{\left(\frac{\cos^2\alpha}{r}-\frac{\cos\alpha}{R}\right)+\left(\frac{\cos^2\beta}{r'}-\frac{\cos\beta}{R}\right)\right\}\\
&+\frac{w^3}{2}\left\{\frac{\sin\alpha}{r}\left(\frac{\cos^2\alpha}{r}-\frac{\cos\alpha}{R}\right)+\frac{\sin\beta}{r'}\left(\frac{\cos^2\beta}{r'}-\frac{\cos\beta}{R}\right)\right\}\\
&+\frac{w^4}{2}\left\{\frac{\sin^2\alpha}{r^2}\left(\frac{\cos^2\alpha}{r}-\frac{\cos\alpha}{R}\right)+\frac{\sin^2\beta}{r'^2}\left(\frac{\cos^2\beta}{r'}-\frac{\cos\beta}{R}\right)\right\}\\
&+\frac{w^4}{8R^2}\left\{\left(\frac{1}{r}-\frac{\cos\alpha}{R}\right)+\left(\frac{1}{r'}-\frac{\cos\beta}{R}\right)\right\}\\
&-\frac{w^4}{8}\left\{\frac{1}{r}\left(\frac{\cos^2\alpha}{r}-\frac{\cos\alpha}{R}\right)^2+\frac{1}{r'}\left(\frac{\cos^2\beta}{r'}-\frac{\cos\beta}{R}\right)^2\right\}. \qquad (5)
\end{aligned}$$

For attaining a good imagery, these terms must be eliminated in turn in the ascending order of the power of w. Calculating the value of each term, we can evaluate the degree of perfection of the image. But in this way, we can not answer the problem how to determine the optimum location of the axis of rotation. This problem is treated in the following way. By the approximation of retaining only up to the second order term and neglecting the rest, the expressions (1) and (2) are expanded into the power series of ω as

$$\left.\begin{aligned}
\xi&=R+Y\omega-(R-X)\frac{\omega^2}{2}\\
\eta&=(R-X)\omega+Y\frac{\omega^2}{2}
\end{aligned}\right\} \qquad (6)$$

$$\left.\begin{aligned}
x_0&=Y\omega+X\frac{\omega^2}{2}\\
y_0&=-X\omega+Y\frac{\omega^2}{2}
\end{aligned}\right\}. \qquad (7)$$

The expressions (6) and (7) are substituted into the expressions (3) and (4) and the following results are obtained.

5) H.G. Beutler: J. Opt. Soc. Am., **35**, (1945) 311.

$$\frac{1}{r}=\frac{1}{\rho}\Big[1-\Big(\frac{X}{\rho}\sin\alpha_0-\frac{Y}{\rho}\cos\alpha_0\Big)\omega$$
$$-\Big\{\frac{X^2}{\rho^2}(1-3\sin^2\alpha_0)-\frac{Y^2}{\rho^2}(3\cos^2\alpha_0-1)+\frac{6XY}{\rho^2}\sin\alpha_0\cos\alpha_0$$
$$-\frac{X}{\rho}\cos\alpha_0-\frac{Y}{\rho}\sin\alpha_0\Big\}\frac{\omega^2}{2}\Big] \qquad (8)$$

$$\cos\alpha=\cos\alpha_0\Big[1-\Big(\frac{X}{\rho}\sin\alpha_0+\frac{Y}{\rho}\frac{\sin^2\alpha_0}{\cos\alpha_0}-\tan\alpha_0\Big)\omega$$
$$-\Big\{\frac{X^2}{\rho^2}(1-3\sin^2\alpha_0)+\frac{3Y^2}{\rho^2}\sin^2\alpha_0+\frac{2XY}{\rho^2}(3\cos^2\alpha_0-1)\tan\alpha_0$$
$$-\frac{X}{\rho}\frac{3\cos^2\alpha_0-1}{\cos\alpha_0}-\frac{3Y}{\rho}\sin\alpha_0+1\Big\}\frac{\omega^2}{2}\Big] \qquad (9)$$

$$\sin\alpha=\sin\alpha_0\Big[1+\Big(\frac{X}{\rho}\frac{\cos^2\alpha_0}{\sin\alpha_0}+\frac{Y}{\rho}\cos\alpha_0-\frac{\cos\alpha_0}{\sin\alpha_0}\Big)\omega$$
$$-\Big\{\frac{3X^2}{\rho^2}\cos^2\alpha_0-\frac{Y^2}{\rho^2}(3\cos^2\alpha_0-1)-\frac{2XY}{\rho^2}\frac{1-3\sin^2\alpha_0}{\sin\alpha_0}\cos\alpha_0$$
$$-\frac{3X}{\rho}\cos\alpha_0+\frac{Y}{\rho}\frac{1-3\sin^2\alpha_0}{\sin\alpha_0}+1\Big\}\frac{\omega^2}{2}\Big] \qquad (10)$$

In (8), (9) and (10), only the expressions relating to the incident rays are given, for in Case I the quantities relating to the incident rays and diffracted rays appear in complete symmetry. The expressions for the diffracted rays are easily obtained by substituting r', ρ', β_0 and β for r, ρ, α_0 and α in these expressions respectively.

The coefficient of $w^2/2$ term is obtained by retaining terms up to those involving ω^2 as

$$\Big(\frac{\cos^2\alpha_0}{\rho}-\frac{\cos\alpha_0}{R}\Big)\Big[1-\Big(\frac{3X}{\rho}\sin\alpha_0-\frac{Y}{\rho}\frac{1-3\sin^2\alpha_0}{\cos\alpha_0}-2\frac{\sin\alpha_0}{\cos\alpha_0}\Big)\omega$$
$$-\Big\{\frac{3X^2}{\rho^2}(1-5\sin^2\alpha_0)-\frac{Y^2}{\rho^2}\frac{2-15\sin^2\alpha_0\cos^2\alpha_0}{\cos^2\alpha_0}+\frac{6XY}{\rho^2}(5\cos^2\alpha_0-2)\frac{\sin\alpha_0}{\cos\alpha_0}$$
$$-\frac{5X}{\rho}\frac{1-3\sin^2\alpha_0}{\cos\alpha_0}-\frac{Y}{\rho}(11-15\sin^2\alpha_0)\frac{\sin\alpha_0}{\cos^2\alpha_0}+\frac{2\cos2\alpha_0}{\cos^2\alpha_0}\Big\}\frac{\omega^2}{2}\Big]$$
$$-\frac{\cos\alpha_0}{R}\Big[\Big(\frac{2X}{\rho}\sin\alpha_0-\frac{Y}{\rho}\frac{\cos2\alpha_0}{\cos\alpha_0}-\frac{\sin\alpha_0}{\cos\alpha_0}\Big)\omega$$
$$+\Big\{\frac{2X^2}{\rho^2}(1-6\sin^2\alpha_0)-\frac{2Y^2}{\rho^2}\frac{1-6\sin^2\alpha_0\cos^2\alpha_0}{\cos^2\alpha_0}+\frac{2XY}{\rho^2}(12\cos^2\alpha_0-5)\frac{\sin\alpha_0}{\cos\alpha_0}$$
$$-\frac{3X}{\rho}\frac{1-4\sin^2\alpha_0}{\cos\alpha_0}-\frac{4Y}{\rho}\frac{2-3\sin^2\alpha_0}{\cos^2\alpha_0}\sin\alpha_0+1-2\frac{\sin^2\alpha_0}{\cos^2\alpha_0}\Big\}\frac{\omega^2}{2}\Big]$$

+(the expression obtained by replacing ρ, α_0 in the preceding terms by ρ', β_0) . (11)

The coefficient of $w^3/2$ term in (5) is calculated up to ω term as

$$\frac{\sin\alpha_0}{\rho}\left(\frac{\cos^2\alpha_0}{\rho}-\frac{\cos\alpha_0}{R}\right)$$
$$+\frac{\sin\alpha_0}{\rho}\left[\left(\frac{\cos^2\alpha_0}{\rho}-\frac{\cos\alpha_0}{R}\right)\left\{\frac{X}{\rho}\frac{1-3\sin^2\alpha_0}{\sin\alpha_0}+\frac{Y}{\rho}\frac{3\cos^2\alpha_0-1}{\cos\alpha_0}-\frac{\cos 2\alpha_0}{\sin\alpha_0\cos\alpha_0}\right\}\right.$$
$$\left.-\frac{\cos^2\alpha_0}{\rho}\left(\frac{2X}{\rho}\sin\alpha_0-\frac{Y}{\rho}\frac{\cos 2\alpha_0}{\cos\alpha_0}-\frac{\sin\alpha_0}{\cos\alpha_0}\right)\right]\omega$$

+(the expression obtained by replacing ρ, α_0 in the preceding terms by ρ', β_0) . (12)

2.2 Calculation for Case II

In Case II, the principal ray of either incident or emergent bundle is fixed in the space. As the concave grating is rotated for changing the wavelength, the point of incidence of the principal ray moves on the grating surface.

The Beutler's expressions are in expanded form referred to coordinates on the plane tangential to the grating surface at the vertex, on which plane the grooves are ruled in equal intervals. Since the principal ray does not always fall at the vertex, the coordinates must be transformed to those on the tangential plane at the point of incidence.

In Fig. 2, let

P: an arbitrary point on the concave grating,

$G_0(x_0, y_0)$: the vertex of the concave grating,

$G'(x, y)$: the point of incidence of the principal ray.

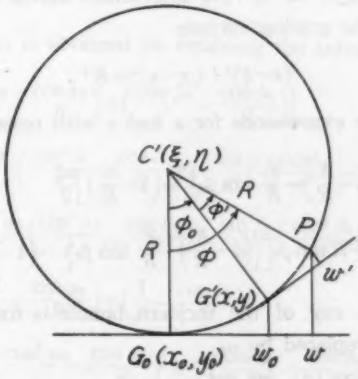

Fig. 2

Let the coordinates of P and G' referred to the tangent at G_0 be w and w_0 respectively, and the coordinate of P referred to the tangent at G' be w', then

$$w=R\sin\phi\,,\qquad w_0=R\sin\phi_0\,,\qquad w'=R\sin\phi'$$
$$\phi=\phi'+\phi_0$$

$$w=w'\cos\phi_0+w_0\cos\phi'=w'\sqrt{1-\frac{w_0^2}{R^2}}+w_0\sqrt{1-\frac{w'^2}{R^2}}\,. \tag{13}$$

Expand the square-roots by the binomial theorem. Remembering that w'^2 and w'^3 terms are to be used up to the terms involving ω^2 and ω respectively and w_0 to begin with ω term, and ignoring higher order terms that are considered not needed, we get

$$\left.\begin{aligned} w&=w_0+w'\Big(1-\frac{w_0^2}{2R^2}\Big)-\frac{w_0}{2R^2}\,w'^2\\ w^2&=w_0^2+2w'w_0+w'^2\Big(1-\frac{2w_0^2}{R^2}\Big)-w'^3\frac{w_0}{R}\\ w^3&=w_0^3+3\,w_0^2w'+3\,w_0w'^2+w'^3\\ w^4&=w_0^4+4\,w_0^3w'+6\,w_0^2w'^2+4\,w_0w'^3+w'^4 \end{aligned}\right\}\,. \tag{14}$$

The relation between w_0 and ω is now to be determined. In Fig. 2, let the area of the triangle $\Delta C'G_0G'$ be S, then

$$2S=Rw_0=(x-x_0)(\eta-y_0)-(\xi-x_0)(y-y_0)\,. \tag{15}$$

Let us assume in the following that the principal ray of emergent bundle is fixed. The equation representing the principal ray is given as

$$y=x\tan\beta_0\,. \tag{16}$$

The coordinates $(x,\ y)$ of G' are determined as the intersection point of the straight line (16) and the grating surface

$$(x-\xi)^2+(y-\eta)^2=R^2\,. \tag{17}$$

After expanding the expressions for x and y with respect to ω, we obtain

$$\left.\begin{aligned} x&=Y\omega+R\Big[\Big\{\Big(1-\frac{X}{R}\Big)-\frac{Y}{R}\tan\beta_0\Big\}^2-\Big(1-\frac{X}{R}\Big)\Big]\frac{\omega^2}{2}\\ y&=Y\tan\beta_0\cdot\omega+R\tan\beta_0\Big[\Big\{\Big(1-\frac{X}{R}\Big)-\frac{Y}{R}\tan\beta_0\Big\}^2-\Big(1-\frac{X}{R}\Big)\Big]\frac{\omega^2}{2} \end{aligned}\right\}\,. \tag{18}$$

When the principal ray of the incident bundle is fixed, β_0 in the expression (16) and (18) must be replaced by α_0.

Substituting (18) into (15), we get

$$\frac{w_0}{R}=-\left(\frac{X}{R}+\frac{Y}{R}\tan\beta_0\right)\omega$$
$$-\left[\left\{\left(1-\frac{X}{R}\right)-\frac{Y}{R}\tan\beta_0\right\}^2\tan\beta_0-\left\{\left(1-\frac{X}{R}\right)\tan\beta_0+\frac{Y}{R}\right\}\right]\frac{\omega^2}{2}. \quad (19)$$

Substituting (14) into w in the expression (5) and rearranging the terms according to the order in w', we have for the coefficient of w' term

$$-\left\{(\sin\alpha+\sin\beta)-\frac{m\lambda}{d}\right\}\left(1-\frac{1}{2}\frac{w_0^2}{R^2}\right)$$
$$+w_0\left\{\left(\frac{\cos^2\alpha}{r}-\frac{\cos\alpha}{R}\right)+\left(\frac{\cos^2\beta}{r'}-\frac{\cos\beta}{R}\right)\right\}$$
$$+\frac{3}{2}w_0^2\left\{\frac{\sin\alpha_0}{\rho}\left(\frac{\cos^2\alpha_0}{\rho}-\frac{\cos\alpha_0}{R}\right)+\frac{\sin\beta_0}{\rho'}\left(\frac{\cos^2\beta_0}{\rho'}-\frac{\cos\beta_0}{R}\right)\right\}. \quad (20)$$

The coefficient of w'^2 term is obtained by retaining the terms of up to ω^2,

$$\frac{w_0}{2R^2}\left\{(\sin\alpha+\sin\beta)-\frac{m\lambda}{d}\right\}$$
$$+\frac{1}{2}\left(1-\frac{2w_0^2}{R^2}\right)\left\{\left(\frac{\cos^2\alpha}{r}-\frac{\cos\alpha}{R}\right)+\left(\frac{\cos^2\beta}{r'}-\frac{\cos\beta}{R}\right)\right\}$$
$$+\frac{3}{2}w_0\left\{\frac{\sin\alpha}{r}\left(\frac{\cos^2\alpha}{r}-\frac{\cos\alpha}{R}\right)+\frac{\sin\beta}{r'}\left(\frac{\cos^2\beta}{r'}-\frac{\cos\beta}{R}\right)\right\}$$
$$+3w_0^2\left\{\frac{\sin^2\alpha_0}{\rho^2}\left(\frac{\cos^2\alpha_0}{\rho}-\frac{\cos\alpha_0}{R}\right)+\frac{\sin^2\beta_0}{\rho'^2}\left(\frac{\cos^2\beta_0}{\rho'}-\frac{\cos\beta_0}{R}\right)\right\}$$
$$+\frac{3w_0^2}{4R^2}\left\{\left(\frac{1}{\rho}-\frac{\cos\alpha_0}{R}\right)+\left(\frac{1}{\rho'}-\frac{\cos\beta_0}{R}\right)\right\}$$
$$-\frac{3}{4}w_0^2\left\{\frac{1}{\rho}\left(\frac{\cos^2\alpha_0}{\rho}-\frac{\cos\alpha_0}{R}\right)^2+\frac{1}{\rho'}\left(\frac{\cos^2\beta_0}{\rho'}-\frac{\cos\beta_0}{R}\right)^2\right\}. \quad (21)$$

The coefficient of w'^3 term is obtained by retaining the terms of up to ω,

$$-\frac{w_0}{2R^2}\left\{\left(\frac{\cos^2\alpha_0}{\rho}-\frac{\cos\alpha_0}{R}\right)+\left(\frac{\cos^2\beta_0}{\rho'}-\frac{\cos\beta_0}{R}\right)\right\}$$
$$+\frac{1}{2}\left\{\frac{\sin\alpha}{r}\left(\frac{\cos^2\alpha}{r}-\frac{\cos\alpha}{R}\right)+\frac{\sin\beta}{r'}\left(\frac{\cos^2\beta}{r'}-\frac{\cos\beta}{R}\right)\right\}$$
$$+2w_0\left\{\frac{\sin^2\alpha_0}{\rho^2}\left(\frac{\cos^2\alpha_0}{\rho}-\frac{\cos\alpha_0}{R}\right)+\frac{\sin^2\beta_0}{\rho'^2}\left(\frac{\cos^2\beta_0}{\rho'}-\frac{\cos\beta_0}{R}\right)\right\}$$
$$+\frac{w_0}{2R^2}\left\{\left(\frac{1}{\rho}-\frac{\cos\alpha_0}{R}\right)+\left(\frac{1}{\rho'}-\frac{\cos\beta_0}{R}\right)\right\}$$
$$-\frac{w_0}{2}\left\{\frac{1}{\rho}\left(\frac{\cos^2\alpha_0}{\rho}-\frac{\cos\alpha_0}{R}\right)^2+\frac{1}{\rho'}\left(\frac{\cos^2\beta_0}{\rho'}-\frac{\cos\beta_0}{R}\right)^2\right\}. \quad (22)$$

§ 3. Discussions of Results

To form an image by the bundle of rays lying in the meridional plane, the terms of the expression (5) derived from the Beutler's expression must vanish in turn in the ascending order of w. The higher the order of the term that vanishes, the more perfect the imagery.

3.1 Discussion of Case I

At first, equating the coefficient of w term in (5) to zero, we get

$$d(\sin\alpha+\sin\beta)=m\lambda\,. \tag{23}$$

This is an equation determining the wavelength of the diffracted rays and need not be regarded as the condition for imagery. m is an integer either positive or negative giving the order of spectral line. Substituting the expression (10) and the corresponding one for emergent rays into (23), we get the expression for the wavelength λ of diffracted rays which pass through the exit slit when the grating is rotated around the point (X, Y) through an angle ω. Then, equating the w^2 term, that is the term of zero order with respect to ω in the equation (8), to zero, we obtain

$$\left(\frac{\cos^2\alpha_0}{\rho}-\frac{\cos\alpha_0}{R}\right)+\left(\frac{\cos^2\beta_0}{\rho'}-\frac{\cos\beta_0}{R}\right)=0\,. \tag{24}$$

This equation can be satisfied by the Rowland condition $\rho=R\cos\alpha_0$, $\rho'=R\cos\beta_0$. But we regard it as a special case and consider in the following the general type of mounting which satisfys the condition (24) at the beginning of rotation.

Here we are at a parting to decide which terms we should consider important for further discussion.

Seya was concerned about w^2, $w^2\omega$ and $w^2\omega^2$ terms, while Onaka dealt with w^2 and $w^2\omega$ terms for the mounting which satisfys the Rowland condition at the beginning.

For the mounting of general type (24) which does not satisfy the Rowland condition, it is desirable to make the w^3 term negligible for good imagery with a grating of a large width.

Therefore putting the w^3 term equal to zero, we get

$$\frac{\sin\alpha_0}{\rho}\left(\frac{\cos^2\alpha_0}{\rho}-\frac{\cos\alpha_0}{R}\right)+\frac{\sin\beta_0}{\rho'}\left(\frac{\cos^2\beta_0}{\rho'}-\frac{\cos\beta_0}{R}\right)=0\,. \tag{25}$$

We obtain as the condition satisfying (24) and (25) simultaneously,

$$\left(\frac{\sin\alpha_0}{\rho}-\frac{\sin\beta_0}{\rho'}\right)\left(\frac{\cos^2\alpha_0}{\rho}-\frac{\cos\alpha_0}{R}\right)=0\,. \tag{26}$$

Two cases are obtained as the solutions of (26).

i) $\rho=R\cos\alpha_0$, $\rho'=R\cos\beta_0$. This is the Rowland condition and we regard it as a special case mentioned above.

ii)
$$\frac{\sin\alpha_0}{\rho}=\frac{\sin\beta_0}{\rho'}\,. \tag{27}$$

Putting (27) into (24), we get

$$\left.\begin{aligned}\frac{1}{\rho}&=\frac{\sin\beta_0}{R}\,\frac{\cos\alpha_0+\cos\beta_0}{(\sin\alpha_0+\sin\beta_0)(1-\sin\alpha_0\sin\beta_0)}\\ \frac{1}{\rho'}&=\frac{\sin\alpha_0}{R}\,\frac{\cos\alpha_0+\cos\beta_0}{(\sin\alpha_0+\sin\beta_0)(1-\sin\alpha_0\sin\beta_0)}\end{aligned}\right\}. \tag{28}$$

On the type of mounting given by (28), no information seemed available in literature, so this case is taken up and discussed below in detail.

1) If we assume $\alpha_0=\beta_0$, then

$$\rho=\rho'=R\cos\alpha_0\,. \tag{29}$$

This is the case known as the Eagle mounting which of course conforms to the Rowland condition. Therefore the Eagle mounting belongs to the mounting (28).

2) When $\alpha_0=0$ or $\beta_0=0$,

$$\left.\begin{aligned}&\frac{1}{\rho}=\frac{1+\cos\beta_0}{R}\,,\quad \frac{1}{\rho'}=0\\ \text{or}\quad &\frac{1}{\rho}=0\,,\quad \frac{1}{\rho'}=\frac{1+\cos\alpha_0}{R}\end{aligned}\right\}. \tag{30}$$

Wadsworth mounting belongs to the mounting (28).

3) Supposing $\rho=R\cos\alpha_0$. $\rho'=R\cos\beta_0$, we obtain

$$\tan\alpha_0=\tan\beta_0\,,\qquad \therefore\quad \alpha_0=\beta_0\,. \tag{31}$$

The Eagle mounting is the only mounting that belongs to (28) and conforms to the Rowland condition.

4) If $\sin\alpha_0\cdot\sin\beta_0<0$, then $\rho\cdot\rho'<0$. Therefore, if the incident ray is on the one side and the emergent ray is on the other side of the grating normal, either exit or entrance slit must be virtual. To make both the entrance and exit slits real, the incident and diffracted rays must be on the same side of the normal.

5) This mounting can not give sharp spectral lines for some wavelength region on a photographic plate contrary to the mounting conforming to the Rowland condition, for, with fixed ρ and α_0, ρ' and β_0 are determined uniquely by (28) and it is impossible for other wavelength to match the condition (28). But even if the wavelength λ is given, there are a number of combinations of α_0 and β_0 and definite

values of ρ and ρ' for every combination. Therefore there remains the possibility of applying this mounting to photoelectric-spectrometric use. We need only to find the position of the axis of rotation which hold the relation (28) valid during the rotation.

Then, the condition for the coefficient of $w^3\omega$ term to become zero is obtained as follows.

$$-X\left\{\frac{\sin\alpha_0}{\rho}\left(\frac{3\cos^2\alpha_0}{\rho}-\frac{\cos\alpha_0}{R}\right)+\frac{\sin\beta_0}{\rho'}\left(\frac{3\cos^2\beta_0}{\rho'}-\frac{\cos\beta_0}{R}\right)\right\}$$
$$+Y\left\{\frac{1-3\sin^2\alpha_0}{\rho}\frac{\cos\alpha_0}{\rho}+\frac{\sin^2\alpha_0}{\rho}\frac{1}{R}+\frac{1-3\sin^2\beta_0}{\rho'}\frac{\cos\beta_0}{\rho'}+\frac{\sin^2\beta_0}{\rho'}\frac{1}{R}\right\}$$
$$+\sin\alpha_0\left(\frac{2\cos\alpha_0}{\rho}-\frac{1}{R}\right)+\sin\beta_0\left(\frac{2\cos\beta_0}{\rho'}-\frac{1}{R}\right)=0\ . \tag{32}$$

This is an equation representing a straight line. By taking a point on this straight line as the centre of rotation, the $w^3\omega$ term can be made to vanish and by removing the point to the infinity, the linear displacement of the grating perpendicular to this straight line may be adopted in place of the rotation.

On the supposition of the Rowland condition being satisfied at the start, the equation (32) becomes

$$\frac{2X}{R}+\frac{Y}{R}\frac{\cos\alpha_0+\cos\beta_0}{\sin\alpha_0+\sin\beta_0}\frac{1-2\cos\alpha_0\cos\beta_0}{\cos\alpha_0\cos\beta_0}=1\ . \tag{33}$$

This is a straight line passing the centre of the Rowland circle ($R/2$, 0). Assuming that the centre of rotation is located on the straight line perpendicular to the bisecting line of the angle between incident and emergent rays at the beginning, we have, after some calculation, for the distance l of the centre of rotation from the vertex as,

$$l=-R\sin\frac{\alpha_0+\beta_0}{2}\Big/\left\{1-\tan\frac{\alpha_0-\beta_0}{2}(\tan\alpha_0-\tan\beta_0)/2\right\}\ . \tag{34}$$

This agrees with the result obtained by Onaka.

For the mounting which follows the condition (28), we obtain the equation corresponding to (33) by substituting (28) into (32).

The condition which makes the $w^5\omega$ term equal to naught is derived from (12) as

$$\frac{\sin\alpha_0}{\rho}\left(\frac{\cos^2\alpha_0}{\rho}-\frac{\cos\alpha_0}{R}\right)\left\{\frac{X}{\rho}\frac{1-3\sin^2\alpha_0}{\sin\alpha_0}+\frac{Y}{\rho}\frac{3\cos^2\alpha_0-1}{\cos\alpha_0}-\frac{\cos 2\alpha_0}{\sin\alpha_0\cos\alpha_0}\right\}$$

$$+\frac{\sin\beta_0}{\rho'}\left(\frac{\cos^2\beta_0}{\rho'}-\frac{\cos\beta_0}{R}\right)\left\{\frac{X}{\rho'}\frac{1-3\sin^2\beta_0}{\sin\beta_0}+\frac{Y}{\rho'}\frac{3\cos^2\beta_0-1}{\cos\beta_0}-\frac{\cos 2\beta_0}{\sin\beta_0\cos\beta_0}\right\}$$

$$-\frac{\sin\alpha_0\cos^2\alpha_0}{\rho'}\left(\frac{2X}{\rho}\sin\alpha_0-\frac{Y}{\rho}\frac{\cos 2\alpha_0}{\cos\alpha_0}-\tan\alpha_0\right)$$

$$-\frac{\sin\beta_0\cos^2\beta_0}{\rho'^2}\left(\frac{2X}{\rho'}\sin\beta_0-\frac{Y}{\rho'}\frac{\cos 2\beta_0}{\cos\alpha_0}-\tan\beta_0\right)=0. \qquad (35)$$

The locus of the centre of rotation (X, Y) expressed by (35) is a straight line. When the Rowland condition is satisfied at the beginning, (35) becomes

$$\frac{2X}{R}-\frac{Y}{R}\frac{\sin\alpha_0+\sin\beta_0}{\cos\alpha_0+\cos\beta_0}\frac{\cos\alpha_0\cos\beta_0}{1-\cos\alpha_0\cos\beta_0}\left(2-\frac{1-\sin\alpha_0\sin\beta_0}{\cos^2\alpha_0\cos^2\beta_0}\right)=1. \qquad (36)$$

This represents a straight line passing through the centre of the Rowland circle $(R/2, 0)$. It intersects at the centre of the Rowland circle with the locus (33) which makes the $w^3\omega$ term equal to zero; there is no other common point. In a special case in which (33) and (36) express one and the same straight line, any point on it can be used as the centre of rotation to make the $w^3\omega$ and $w^3\omega$ terms simultaneously to zero, provided that the direction cosines of (33) and (36) are the same. As the necessary condition for this to happen, calculation gives the following expression

$$\cos(\alpha_0-\beta_0)\{\cos(\alpha_0-\beta_0)-1\}=0, \qquad (37)$$

that is,

$$|\alpha_0-\beta_0|=\pi/2 \text{ or } \alpha_0-\beta_0=0. \qquad (38)$$

The one is the Eagle mounting, in which the incident and emergent rays are in the same direction, and the other is the mounting in which they are at right angle. We refer the latter as "Diametrical mounting".

In these mountings, both (33) and (36) become

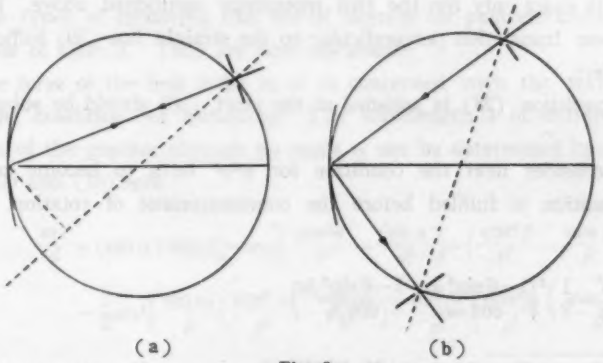

(a) (b)

Fig. 3

$$\frac{X}{R}-\frac{Y}{R}\frac{\cos 2\alpha_0}{\sin 2\alpha_0}=\frac{1}{2}, \tag{39}$$

which represents a straight line connecting the entrance slit and the centre of the Rowland circle as shown in Fig. 3 (a) and (b).

By locating the entrance and exit slits either separately on the two intersections of two arbitrary Rowland circles or jointly on one of them, the Rowland condition can be fulfiled at two wavelengths. In these cases, the centre of rotation should be on the straight line connecting two points of intersection of the two Rowland circles as can be understood on Fig. 4.

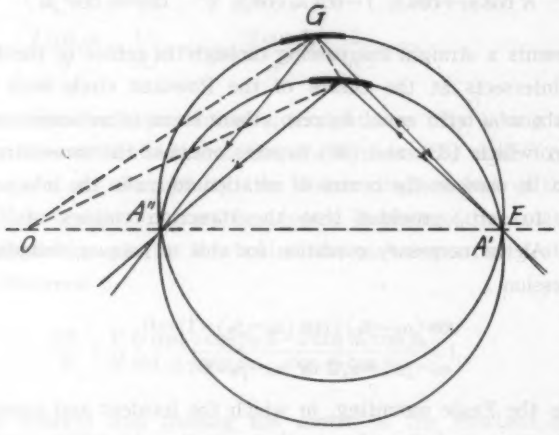

Fig. 4

This was found by Johnson[6] on the near-Eagle mountings using an approximation, and it is exact only for the two mountings mentioned above. In place of rotation, linear translation perpendicular to the straight line (39) suffices to cause the same effect.

If the condition (28) is satisfied at the start, (28) should be substituted into (35).

Let us consider next the condition for $w^3\omega^3$ term to become zero. If the Rowland condition is fulfiled before the commencement of rotation, we obtain from (11),

$$\left(\frac{X}{R}-\frac{1}{2}\right)^2\left\{\frac{1-6\sin^2\alpha_0}{\cos\alpha_0}+\frac{1-6\sin^2\beta_0}{\cos\beta_0}\right\}$$

6) P.D. Johnson: Rev. Sci. Inst., **28**, (1957) 833.

$$+\left(\frac{X}{R}-\frac{1}{2}\right)\frac{Y}{R}\left\{\frac{(12\cos^2\alpha_0-5)\sin\alpha_0}{\cos^2\alpha_0}+\frac{(12\cos^2\beta_0-5)\sin\beta_0}{\cos^2\beta_0}\right\}$$

$$-\frac{Y^2}{R^2}\left\{\frac{1-6\sin^2\alpha_0\cos^2\alpha_0}{\cos^3\alpha_0}+\frac{1-6\sin^2\beta_0\cos^2\beta_0}{\cos^3\beta_0}\right\}$$

$$-\frac{1}{2}\left(\frac{X}{R}-\frac{1}{2}\right)\left(\frac{1}{\cos\alpha_0}+\frac{1}{\cos\beta_0}\right)-\frac{1}{2}\frac{Y}{R}\left(\frac{\sin\alpha_0}{\cos^2\alpha_0}+\frac{\sin\beta_0}{\cos^2\beta_0}\right)=0. \qquad (40)$$

This is an equation of a conic section passing the centre of the Rowland circle $(R/2, 0)$. The point of intersection of (33) and (40) gives the centre of rotation to make the $w^2\omega$ and $w^2\omega^2$ terms equal to zero simultaneously. In general, a straight line intersects a conic section at two points. Hence the intersection of (33) and (40) gives one more point other than the centre of the Rowland circle. It is not easy to determine analytically the position of this point.

The locus of the centre of rotation in the mountings belonging to (28) is determined from (28) and the ω^2 term of (11). It is also a conic section.

Starting from the general type of mounting satisfying (24), calculation gives the mountings comparable with Seya mounting for any given value of $C=\alpha_0-\beta_0$ but the centre of rotation departs from the grating vertex.

So far the outline of the theory of mounting for the Case I is presented. In Case I, if one starts from the Rowland condition and rotates the grating about the centre of the Rowland circle, the condition for imagery is satisfied to higher terms showing that the mounting is excellent. Therefore the various types of mounting mentioned above for Case I are of interest only when, for some reason, the centre of the Rowland circle is not used as the centre of rotation. The directions of incident and emergent rays change in Case I as mentioned already, and therefore the application of Case I to photoelectric-spectrometric use will be met with some difficulty.

3.2 Discussion of Case II

The types of mounting that are of interest for photoelectric-spectrometric use are those of Case II. They are now discussed.

The term of the first order in w' is concerned with the wavelength but not with the condition for mounting. The wavelength λ of diffracted ray after the rotation of the grating through an angle ω can be determined by substituting (8), (9), (10) and (19) into

$$\frac{m\lambda}{d}=(\sin\alpha+\sin\beta)-w_0\left\{\left(\frac{\cos^2\alpha}{r}-\frac{\cos\alpha}{R}\right)+\left(\frac{\cos^2\beta}{r'}-\frac{\cos\beta}{R}\right)\right\}$$

$$-\frac{3}{2}w_0^2\left\{\frac{\sin\alpha_0}{\rho}\left(\frac{\cos^2\alpha_0}{\rho}-\frac{\cos\alpha_0}{R}\right)+\frac{\sin\beta_0}{\rho'}\left(\frac{\cos^2\beta_0}{\rho'}-\frac{\cos\beta_0}{R}\right)\right\}. \qquad (41)$$

Equating the w'^2 term to zero, we get the same equation as (24). This is the

condition for imagery at the start and therefore must be satisfied by all the mountings that are considered below.

Making the w'^3 term equal to zero, we obtain (25) from (22). This means also the condition for imagery at the start and is satisfied by the two mountigs, one conforming to the Rowland condition and the other to the condition (28).

Let us consider the $w'^2\omega$ term next.

According to (41), $(\sin\alpha+\sin\beta)-m\lambda/d$ begins with the term of the first order in ω. As the mountings considered in the following satisfy the condition (24) at the start, the coefficient of the ω term in (41) becomes zero and only the terms higher than ω^2 remain. Therefore in discussing the $w'^2\omega$ and $w'^2\omega^2$ terms, the first term of (21) need not be taken into account.

The condition obtained by equating the $w'^2\omega$ term of (21) to zero is, after some calculation, as follows:

$$
\begin{aligned}
&-X\left\{\frac{\sin\alpha_0}{\rho}\left(\frac{3\cos^2\alpha_0}{\rho}-\frac{\cos\alpha_0}{R}\right)+\frac{\sin\beta_0}{\rho'}\left(\frac{3\cos^2\beta_0}{\rho'}-\frac{\cos\beta_0}{R}\right)\right\}\\
&\quad+Y\left\{\frac{1-3\sin^2\alpha_0}{\rho}\frac{\cos\alpha_0}{\rho}+\frac{\sin^2\alpha_0}{\rho}\frac{1}{R}+\frac{1-3\sin^2\beta_0}{\rho'}\frac{\cos\beta_0}{\rho'}+\frac{\sin^2\beta_0}{\rho'}\frac{1}{R}\right\}\\
&\quad+\sin\alpha_0\left(\frac{2\cos\alpha_0}{\rho}-\frac{1}{R}\right)+\sin\beta_0\left(\frac{2\cos\beta_0}{\rho'}-\frac{1}{R}\right)\\
&\quad-3(X+Y\tan\beta_0)\left\{\frac{3\sin\alpha_0}{\rho}\left(\frac{\cos^2\alpha_0}{\rho}-\frac{\cos\alpha_0}{R}\right)+\frac{3\sin\beta_0}{\rho'}\left(\frac{\cos^2\beta_0}{\rho'}-\frac{\cos\beta_0}{R}\right)\right\}=0.
\end{aligned}
\tag{42}
$$

The only difference of this equation from the equation (32) in Case I is the last additional term. As this additional term becomes zero in the two mountings, one conforming to the Rowland circle and the other to the condition (28), the above condition (42) becomes the same as the condition in Case I. But in the more general types of mounting satisfying only (24), the condition (42) differs from the one in Case I.

We consider the $w'^3\omega$ term next. In discussing this term, only the mountings satisfying the Rowland condition or the condition (28) are of significance. Taking this into account, we obtain from (22) the condition for the $w'^3\omega$ term to become zero as

$$
\begin{aligned}
&X\left\{\frac{1}{\rho^3}\left(\frac{\cos^3\alpha}{\rho}-\frac{\cos\alpha_0}{R}\right)+\frac{1}{\rho'^3}\left(\frac{\cos^3\beta_0}{\rho'}-\frac{\cos\beta_0}{R}\right)\right\}\\
&\quad+Y\left\{\frac{3\cos^2\alpha_0-1}{\rho^3}\tan\alpha_0\left(\frac{\cos^2\alpha_0}{\rho}-\frac{\cos\alpha_0}{R}\right)+\frac{3\cos^2\beta_0-1}{\rho'^3}\tan\beta_0\left(\frac{\cos^2\beta_0}{\rho'}-\frac{\cos\beta_0}{R}\right)\right\}
\end{aligned}
$$

$$-\frac{\cos 2\alpha_0}{\rho\cos\alpha_0}\left(\frac{\cos^2\alpha_0}{\rho}-\frac{\cos\alpha_0}{R}\right)-\frac{\cos 2\beta_0}{\rho'\cos\beta_0}\left(\frac{\cos^2\beta_0}{\rho'}-\frac{\cos\beta_0}{R}\right)$$

$$-2X\left(\frac{\sin^2\alpha_0\cos^2\alpha_0}{\rho^3}+\frac{\sin^2\beta_0\cos^2\beta_0}{\rho'^3}\right)$$

$$+Y\left(\frac{\sin\alpha_0\cos\alpha_0\cos 2\alpha_0}{\rho^3}+\frac{\sin\beta_0\cos\beta_0\cos 2\beta_0}{\rho'^3}\right)$$

$$+\frac{\sin^2\alpha_0\cos\alpha_0}{\rho^3}+\frac{\sin^2\beta_0\cos\beta_0}{\rho'^3}$$

$$+(X+Y\tan\beta_0)\left[\frac{1}{\rho}\left(\frac{\cos^2\alpha_0}{\rho}-\frac{\cos\alpha_0}{R}\right)^2+\frac{1}{\rho'}\left(\frac{\cos^2\beta_0}{\rho'}-\frac{\cos\beta_0}{R}\right)^2\right.$$

$$\left.-\frac{1}{R^2}\left\{\left(\frac{1}{\rho}-\frac{\cos\alpha_0}{R}\right)+\left(\frac{1}{\rho'}-\frac{\cos\beta_0}{R}\right)\right\}\right]=0. \qquad (43)$$

This is an equation equal to (35) in Case I except the additional term multiplied by $(X+Y\tan\beta_0)$ in (43). This additional term does not disappear generally and therefore (43) differs from (35).

When the Rowland condition is satisfied at the start, (43) becomes

$$\frac{Y}{R}\left\{\frac{\sin\alpha_0+\sin\beta_0}{\cos\alpha_0+\cos\beta_0}\frac{2\cos^2\alpha_0\cos^2\beta_0+\sin\alpha_0\sin\beta_0-1}{\cos\alpha_0\cos\beta_0(1-\cos\alpha_0\cos\beta_0)}-\tan\beta_0\right\}=3\left(\frac{X}{R}-\frac{1}{3}\right), \qquad (44)$$

which represents a straight line passing through the point $(R/3, 0)$. The point of intersection of (33) and (44) is the centre of rotation corresponding to the centre of the Rowland circle in Case I and reducing both the $w'^2\omega$ and $w'^3\omega$ terms to zero.

The case, in which the loci of the centres of rotation, which reduce $w'^3\omega$ and $w'^3\omega$ terms respectively to zero, coincide, occurs only when both loci coincide also with X-axis, because (33) and (44) always pass through the points $(R/2, 0)$ and $(R/3, 0)$ respectively. Then it should be $\alpha_0=-\beta_0$ as evident from (33) and furthermore $\alpha_0=\beta_0=0$ from (44). Therefore, there is no solution in Case II to satisfy the above-mentioned condition.

In the case of mounting pertaining to (28), we should substitute (28) into (43). The point of intersection of the equation obtained by substituting (28) into (32) and the one obtained above, is the point of rotation that reduces the $w'^2\omega$ and $w'^3\omega$ terms simultaneously to zero for the mounting (28).

The condition for the $w'^2\omega^2$ term to become zero is given for the mounting conforming to the Rowland condition at the start by adding the following terms to (40)

$$-3\left(\frac{X}{R}+\frac{Y}{R}\tan\beta_0\right)\left\{\frac{2X}{R}\left(\frac{\sin^2\alpha_0}{\cos\alpha_0}+\frac{\sin^2\beta_0}{\cos\beta_0}\right)-\frac{Y}{R}\left(\frac{\sin\alpha_0\cos 2\alpha_0}{\cos^2\alpha_0}+\frac{\sin\beta_0\cos 2\beta_0}{\cos^2\beta_0}\right)\right.$$
$$\left.-\left(\frac{\sin^2\alpha_0}{\cos\alpha_0}+\frac{\sin^2\beta_0}{\cos\beta_0}\right)\right\}-\frac{3}{2}\left(\frac{X}{R}+\frac{Y}{R}\tan\beta_0\right)^2\left(\frac{\sin^2\alpha_0}{\cos\alpha_0}+\frac{\sin^2\beta_0}{\cos\beta_0}\right). \qquad (45)$$

This represents a conic section. In general, the straight line (33) intersects this conic section at two points. Taking one of the points as the centre of rotation, we obtain a mounting of good imaging performance for a wide range of wavelength. Although it satisfys the Rowland condition at the start, it will soon become otherwise and therefore we cannot regard it as a mounting better than Seya's.

§ 4. Astigmatism

Thus far, the image formation by the bundle of rays lying in the meridional plane alone has been considered. The astigmatism is one of substantial defects of the concave grating.

Haber[7] presented the theory on the torus grating which is free from astigmatism at two wavelengths and practically suppresses it in the neighbourhoods of those wavelengths.

Sakayanagi[8] devised a special type of concave grating with circularly curved grooves to remove the astigmatism and produced it to test his theory.

Greiner and Schäffer[9] discussed the astigmatism given by the torus grating and by the spherical grating, and calculated the brightness of spectral line and the light flux emerging from the exit slit.

To complete the theory of mounting the concave grating, the astigmatism is discussed here briefly. The torus grating becomes the spherical grating if the two radii of principal curvatures of the toric surface are equal. Then, we only need to consider the astigmatism of the torus grating. According to Haber, the following equations must be satisfied for eliminating the astigmatism.

$$\frac{\cos^2\alpha_0}{\rho}-\frac{\cos\alpha_0}{R}+\frac{\cos^2\beta_0}{\rho'}-\frac{\cos\beta_0}{R}=0 \qquad (46)$$

$$\frac{1}{\rho}-\frac{\cos\alpha_0}{R^*}+\frac{1}{\rho'}-\frac{\cos\beta_0}{R^*}=0\,. \qquad (47)$$

(46) is the same as (24) that is the condition for imagery by the meridional rays. (47) is the condition for the sagittal rays.

7) H. Haber: J. Opt. Soc. Am., **40**, (1950) 153.
8) Y. Sakayanagi: Science of Light (Tokyo), **3**, (1954) 1.
9) H. Greiner und E. Schäffer: Optik, **16**, (1959) 288.
H. Greiner und E. Schäffer: Optik, **16**, (1959) 350.

Assuming $R^*=R$, we get a set of ρ and ρ' as

$$\left.\begin{aligned}\frac{1}{\rho}&=\frac{1}{R}\frac{\sin^2\beta_0}{\sin\beta_0-\sin\alpha_0}\frac{\cos\alpha_0+\cos\beta_0}{\sin\alpha_0+\sin\beta_0}\\ \frac{1}{\rho'}&=\frac{1}{R}\frac{\sin^2\alpha_0}{\sin\alpha_0-\sin\beta_0}\frac{\cos\alpha_0+\cos\beta_0}{\sin\alpha_0+\sin\beta_0}\end{aligned}\right\}, \tag{48}$$

which eliminate the astigmatism of the spherical grating. However, this set can not be realized by both entrance and exit slits being real at the same time, for ρ and ρ' are of different signs.

If $R\neq R^*$, that is, if it is the torus grating, there remains one more degree of freedom for the mounting and we can determine the value of $P=R^*/R$ according to another condition.

Haber adopted the Rowland condition which satisfies the condition for imagery by the meridional rays and obtained the value

$$R^*/R=\cos\alpha_0\cos\beta_0\,. \tag{49}$$

Adopting (28) instead of the Rowland condition, we obtain the value of P for eliminating the astigmatism as

$$R^*/R=1-\sin\alpha_0\sin\beta_0\,. \tag{50}$$

(50) accords with (49) in the case of Eagle mounting, vz $\alpha_0=\beta_0$, as expected. To find the centre of rotation (X, Y), arround which the grating is rotated through a small angle ω satisfying the equations (46) and (47) simultaneously, (46) and (47) must be expanded into series of ω. The position (X, Y) can be determined as the point of intersection of two straight lines expressed by the ω terms of (46) and (47).

§ 5. Conclusion and Acknowledgement

The conditions for obtaining a good imagery by rotating the grating arround a suitable axis to change the wavelength of diffracted rays are derived from the Beutler's expressions. Only the rays lying in the plane passing the grating vertex and normal to the grooves are considered.

A group of mountings practicable for photoelectric-spectrometric use is found. Both the Eagle mounting and Wadsworth mounting belong to this group as special cases. This group of mountings are derived from the conditions obtained by equating w^2 and w^3 terms of Beutler's expression to zero.

Under the condition for the direction of emergent rays to be kept constant, the formula determining the centre of rotation to render $w^2\omega$ and $w^3\omega$ terms zero

and to give a good image-forming characteristics for some wavelength region is given.

While being engaged in this work, the author continually received most instructive advice from colleagues of Institute for Optical Research, especially from Dr. M. Seya and Dr. R. Onaka. Messrs. T. Katayama and M. Inoue cooperated him in checking the calculations involved in this work. The author wishes to express his hearty thanks to all of them.

Absorption Studies of Metastable Mercury Atoms in Argon-Mercury Discharge Afterglows

Masahiro YOKOYAMA

Institute of Physics, North College, Osaka University.

(Received September 3, 1959)

Abstract

The decay of $6^3P_{2,0}$ metastable mercury atoms have been studied by the optical absorption method in the afterglow of argon-mercury discharge at 300°K. Effective ratio α of the breadth of emission line to that of absorption line is determined by doubling the absorption path length. The populations of $6^3P_{2,0}$ mercury metastable atoms in the absorption tube are evaluated by the concentrations of those atoms obtained from measured absorptions.

1. Introduction

In the previous work, current dependence of metastable mercury atoms in argon-mercury discharge afterglows[1] was investigated with an experiment in which a monochromatic light beam from an emission tube was made to pass through an absorption tube and the output was displayed on a cathode-ray tube as a function of time[2].

The relative absorption of the light beam is a measure of the population of corresponding excited metastable state atoms in the absorption tube. Thus, it is necessary to estimate the relative metastable atom density in the absorption tube from measured fractional absorption. The present paper deals with the experimental determination of effective ratio of the line breadths α by doubling the path length and the transformation of measured absorption into metastable atom concentration.

2. Theory

When all types of broadening except Doppler broadening of emission and absorption spectral lines are ignored, fractional absorption A_α which depends on the relative line breadths is given by the equation[3],

1) M. Yokoyama: Science of Light, 7 (1958) 42.
2) F.A. Grant: Can. Jour. Res. A 28 (1950) 339.
3) A.C.G. Mitchell and M.W. Zemansky: Resonance Radiation and Excited Atoms. (University Press, Cambridge, 1934).

$$A_\alpha=\frac{\int_{-\infty}^{\infty} e^{-(\omega/\alpha)^2}(1-e^{-k_0 l e^{-\omega^2}})d\omega}{\int_{-\infty}^{\infty} e^{-(\omega/\alpha)^2}d\omega} \tag{1}$$

$$=\frac{k_0 l}{\sqrt{1+\alpha^2}}-\frac{(k_0 l)^2}{2!\sqrt{1+2\alpha^2}}+\cdots\cdots-(-1)^n\frac{(k_0 l)^n}{n!\sqrt{1+n\alpha^2}}+\cdots\cdots \tag{2}$$

where l is the length of the absorption path and $\omega=\frac{2(\nu-\nu_0)}{\Delta\nu_D}\sqrt{ln\,2}$. The quantity k_0 is the maximum absorption coefficient when Doppler broadening alone is present and is given by

$$k_0=\frac{2}{\Delta\nu_D}\sqrt{\frac{ln\,2}{\pi}}\frac{\lambda_0^2 g_n}{8\pi g_m}A_{nm}M_m \tag{3}$$

Here, λ_0 is the wavelength corresponding to frequency ν_0, g_m and g_n are the respective statistical weights of states m and n, A_{nm} is the Einstein coefficient for the spontaneous transition from state n to state m and M_m is the number of atoms in state m per. cm^3. Fig. 1 illustrates the relation between the absorption A_α and $k_0 l$ calculated party by the above series, partly by graphical integration and partly by graphical interpolation.

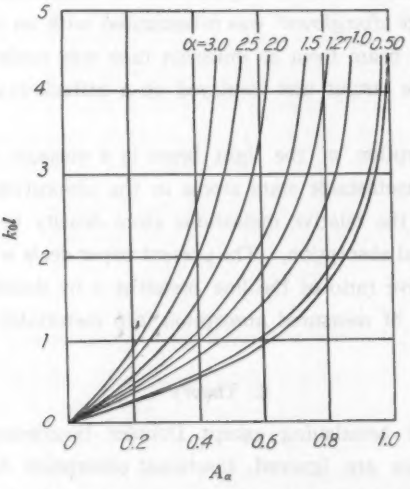

Fig. 1. $k_0 l$ against absorption A_α calculated by equ. (2) by assuming various values of α.

The quantity α is defined by the equation,

$$\alpha=\frac{\text{emission line breadth}}{\text{absorption line breadth}} \tag{4}$$

Now, by using the expression for Doppler breadth:

$$\Delta\nu_D=\frac{2\sqrt{2\,Rln\,2}}{c}\nu_0\sqrt{\frac{T}{M}} \tag{5}$$

where R is the universal gas constant and c is the light velocity. The atom density in the excited state m is given by

$$M_m=\frac{k_0 l}{l}\frac{8\pi\sqrt{2\pi\dfrac{RT}{M}}}{\lambda_0^2 A_{nm}}\frac{g_m}{g_n} \tag{6}$$

3. Experiment

For pure Doppler broadening, the value of α is determined by the gas temperature in the emission and absorption tubes. Since emission and absorption tubes were both excited by square wave pulses of short duration, the average gas temperature was practically the same as that of the walls of the container. Besides, the absorption measurements were made in the late afterglows of the absorption tube. Thus, the emission line breadth corresponded to a higher temperature than that of absorption line. Therefore, the value of α was always greater than unity in the present experimental conditions.

In the present case, doubling of the absorption path length was obtained by exciting the gas first in the first two and then in both end of the three electrodes of the absorption tube. The discharge tube was similar to that employed in the decay measurements of metastable mercury atoms in argon-mercury discharge afterglows. Absorption tube was 4.4 cm inside diameter and 31 cm long in which argon gas of 4 mmHg and mercury of extreme purity were sealed. Three electrodes of the absorption tube were circular rings made of tungsten wire of 0.4 mm or 0.9 mm in diameter, arranged concentric with the walls of the absorption tube.

Optical absorption was measured for two path lengths $l_{\rm I}$ and $l_{\rm II}$ under identical discharge conditions. If the values of the absorption in these two cases are denoted by $A_{\rm I}$ and $A_{\rm II}$, then by plotting the relation $A_{\rm II}$-$A_{\rm I}$ vs $A_{\rm II}$, curves, characteristic of α, will be obtained[4].

Then, the fractional absorption $A_{\rm I}$ for $k_0 l_{\rm I}$ is found by using equ. (2) for a given value of α. In the present case, the ratio between the two actual plasma lengths corresponding to $l_{\rm II}$ and $l_{\rm I}$ in the absorption tube was estimated as 1.6. Thus, the value of $k_0 l_{\rm II}$ is evaluated by multiplying the factor of 1.6 to $k_0 l_{\rm I}$, and the absorption $A_{\rm II}$ against $k_0 l_{\rm II}$ is also obtained by using equ. (2). In Fig. 2,

4) J.R. Dixon and F.A. Grant: Phys. Rev. 107 (1957) 118.

proper relations calculated by the equ. (2) for $A_{II}-A_I$ vs A_{II} by assuming pure Doppler broadening and various α, are plotted.

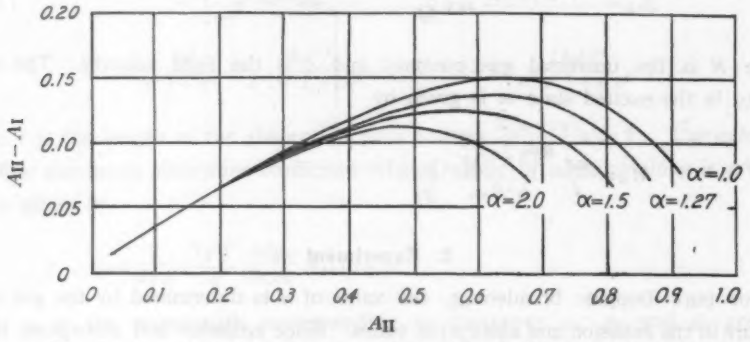

Fig. 2. $A_{II}-A_I$ against A_{II} curves obtained by doubling the absorption path length and evaluated by using equ. (2).

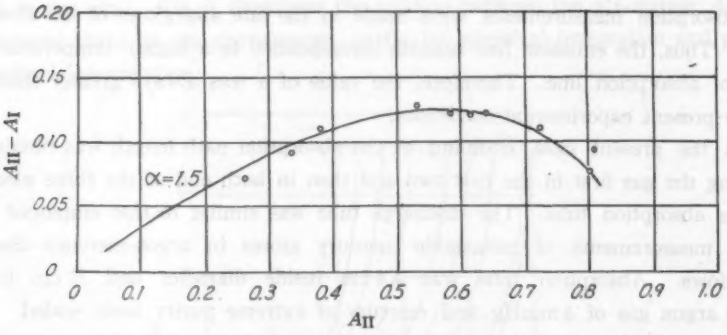

Fig. 3. Experimental plot of λ 5461 Å ($6^3P_2-7^3S_1$) line obtained by doubling the absorption path length.

A typical experimental plot of λ 5461 Å ($6^3P_2-7^3S_1$) mercury line at 300°K is shown in Fig. 3. In this case, current duration in the absorption tube was kept at 0.52 msec. during the measurement of the absorption in the decay. The results well agree with what is shown by the theoretical curve of $\alpha=1.5$ within the limit of the experimental error. The decay plots of λ 5461 Å ($6^3P_2-7^3S_1$) and λ 4047 Å ($6^3P_0-7^3S_1$) mercury lines by assuming $\alpha=1.5$ are shown in Fig. 4 and 5. The choice of $\alpha=1.5$ is for satisfying the foregoing criteria of experimental plot by the doubling of absorption path length.

The distribution of mercury metastable atoms in discharge space of argon-mercury mixtures was investigated by measuring the absorption caused by the metastable atoms. Absorption was measured in an experimental arrangement in

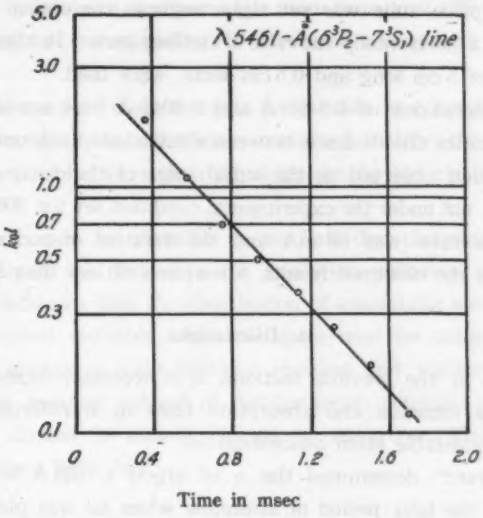

Fig. 4. Decay plot of 6^3P_2 mercury metastable atoms illustrating how the effective $\alpha=1.5$ is determined. λ 5461 Å line. Argon pressure: 4 mmHg.

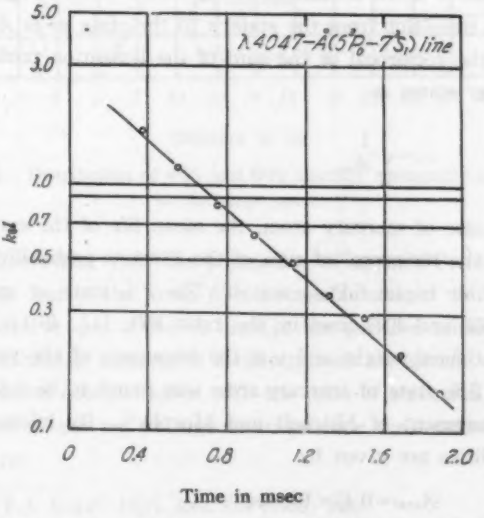

Fig. 5. Decay plot of 6^3P_0 mercury metastable atoms illustrating how the effective $\alpha=1.5$ is chosen. λ 4047 Å line. Argon pressure 4 mmHg.

which the absorption tube was set right angle to the optical axis of the system and mounted on a horizontally movable travelling rack. In this case, two buffles, each with a slit of 5 cm long and 0.5 cm wide, were used.

Measured absorptions of λ 5461-Å and λ 4047-Å lines are shown in Fig. 6, in which abscissa denotes the distance between electrodes in cm unit and ordinate the fractional absorption observed at the initial stage of the decay pattern. Measurement was carried out under the experimental condition set for 300°K. Peak current in the absorption tube was 68 mA and the duration of excitation pulse was 0.3 msec. In plotting the observed results, absorption of less than 5% was neglected.

4. Discussions

As described in the previous sections, it is necessary to estimate the relative line breadth of the emission and absorption lines in transforming the measured absorption into metastable atom concentration.

Futch and Grant[5] determined the α of argon λ 7635 Å line which became a straight line over the later period of afterglow when $k_0 l$ was plotted against time. Phelps and Molnar[6] also determined the effective ratio of the breadths of spectral lines by measuring the absorption in two almost the same absorption cells.

Now, the atom is being considered to have certain probabilities of jumping from an upper state n down to various lower states m emitting radiation. If the probability of the transition from the state n to the state m is A_{nm}, then the mean life is defined as the reciprocal of the sum of the transition probabilities from the state n to all lower states m.

Thus,
$$\tau_n = \frac{1}{\sum_m A_{nm}}$$

Then, in the case of mercury atom, the mean life of the excited 7^3S_1 mercury atom is given by the reciprocal of sum of the Einstein probabilities from 7^3S_1 state to three lower visible triplet $6^3P_{2,1,0}$ states. The 7^3S_1 state of mercury atom will radiate λ 5461, 4358 and 4047 lines in the ratio 100 : 117 : 49 i.e., in the ratio $g\nu^3$, where g is the statistical weight and ν is the frequency of the visible triplet lines[7]. The mean life of 7^3S_1 state of mercury atom was found to be 0.8×10^{-8} sec. by the polarization measurement of Mitchell and Murphy[8]. By taking this value for τ, transition probabilities are given by

$$A_{5461} = 0.47\times10^8 \text{ sec}^{-1}.$$
$$A_{4358} = 0.55\times10^8 \text{ sec}^{-1}.$$
$$A_{4047} = 0.23\times10^8 \text{ sec}^{-1}.$$

Therefore, it is possible to determine the atom density of 6^3P state of mercury atom by estimating $k_0 l$ corresponding to measured absorptions for given values of α.

Most of the absorption measurements were made in a range of pressure and discharge current in which the light beam traversed mainly the positive column of the discharge set up between the ring electrodes by the excitation pulsation in the absorption tube.

From Fig. 6, it may be plausible to conclude that the metastable atoms are distributed uniformly in the plasma by the excitation pulsation in the absorption tube. This effect indicates that the distribution of metastable atoms is also closely connected with emitted radiation. In dark space near the cathode, electrons still have not sufficient energy to make inelastic exciting and ionizing collisions with gas atoms. In the positive column of the discharge, potential gradient is almost constant and the current is mainly carried by electrons. Thus, plasma emits radiation with uniform light flux.

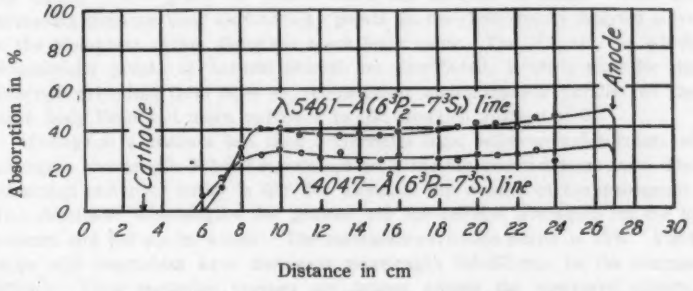

Fig. 6. Distribution of 6^3P_2 and 6^3P_0 mercury metastable atoms in discharge space.

It was also confirmed that the population of upper 6^3P_2 metastable atoms is high compared with that of the lower 6^3P_0 metastable atoms. In Table I, measured absorptions of λ 5461 Å and λ 4047 Å lines in the positive columun at 18 cm from cathode and the calculated metastable concentrations are given. The fact that the ratio of the populations does not agree with the ratio of statistical weights indicates that cnrrent densities are not so high as to produce the saturation of populations of metastable atoms.

5) A.H. Futch and F.A. Grant: Phys. Rev. 104 (1956) 356.
6) A.V. Phelps and J.P. Molnar: Phys. Rev. 89 (1953) 1202.
7) C. Kenty: Jour. Appl. Phys. 21 (1950) 1309.
8) A.C.G. Mitchell and E.J. Murphy: Phys. Rev. 46 (1934) 53.

Table I. Measured absorption and the calculated metastable atom density in plasma.

Lines	Statistical weight	Absorption	M_m(atoms/cc)	Relative ratio
5461	5	0.43	3.0×10^{10}	2
4047	1	0.26	1.5×10^{10}	1

Acknowledgments

The author wishes to express hearty thanks to Prof. T. Asada, Institute of Scientific and Industrial Research, Osaka University, and to Prof. M. Shoda, Institute of Physics, North College, Osaka University, for their encouragement throughout the course of the present experiment. He would also like to thank Prof. K. Honda, Tokyo Electrical Engeneering College and to Prof. S. Kojima, Department of Physics, Tokyo University of Education, for their kind discussions during the course of this investigation.

Apparent Colors of Natural Objects

Hikaru MASAKI

Railway Technical Research Institute, Heibei-shinden, Kokubunji-machi, Tokyo

(Received September 24, 1959)

Summary

Apparent colors of natural objects were measured by three types of telephotometers based on the principles of photoelectric and photographic spectroradiometric methods and visual color matching with a comparison source consisting of an incandescent lamp and three Lovibond glasses. The results are given in terms of CIE chromaticity coordinates, dominant wavelength and excitation purity.

The experimental results show that the apparent colors of natural objects are chiefly yellow-green or yellow when the distance is small. With the increasing distance their chromaticity points on the chromaticity diagram move to the blue-green region along the black body locus. The domain, in which chromaticity points of natural objects are distributed, is fairly wide for the direction extending from blue to yellow-green approximately parallel to the black body locus but much narrower to the direction veatical to it.

Foliage at a distance less than 1 kilometer have yellow-greenish colors of dominant wavelength 542-582 mμ except on a heavily overcast hazy day. The maximum excitation purity is 49% for leaves in the vicinity of the instrument. The dominant wavelengths for grasses are 558-585 mμ, averaging 562 mμ in autumn and 582 mμ in winter. The maximum excitation purity is 45%. Field crops and vegetables have dominant wavelength 561-570 mμ, on the average 565 mμ. Their excitation purities are largest among the measured objects, maximum 52%. Earth color is yellow of the dominant wavelength 561-585 mμ averaging 569 mμ and the maximum excitation purity being 34%. Colors of buildings, water, sky near the horizon, snow surfaces and distant objects are less saturated having the maximum excitation purity of 26%. Their chromaticity points are distributed around the achromatic point. In general natural objects appear more saturated in colors on a clear day than on an overcast day.

These data were applied for discussing the visual range of colored objects and light sources through the atmosphere in the daytime.

1. Introduction

In discussing the visual range of colored objects and light sources through the atmosphere in the daytime, apparent colors of natural objects are one of the important factors because they form the background of the objects or light sources to be discernible and the visual range relates to the color of the background.

Previous researches about this subject known to the author are the work by Nickerson, Kelly and Stultz[1], by Hendley and Hecht[2], and by Penndorf[3]. Nickerson and others compared samples of soils, leaves and grasses with Munsell color cards and obtained the Munsell Hue, Value, and Chroma for them. For some samples spectral reflectances were measured and Munsell-renotations were computed. From these published data we are able to obtain the CIE chromaticity coordinates under the CIE standard Sousce C[4]. Penndorf computed chromaticity coordinates of natural objects under the standard Source B from Krinov's spectrophotometric data. From the above-mentioned reports chromaticity coordinates of natural objects close to the observer illuminated by special standard sources can be obtained. Hendley and Hecht measured the colors of natural objects and terrains by the visual comparison of objects with Munsell color chips and gave chromaticity coordinates for them. They reported colors of objects at various distances, but the chromaticity coordinates given by them were again referred to a special standard source, i.e. the Source C.

On the other hand the author measured directly the apparent colors of natural objects by three types of telephotometers. Measured objects were foliage, grasses, field crops and vegetables; earth, sea, snow surfaces; buildings and sky near the horizon. They were measured at various distances under various weather conditions. The results were expressed in terms of CIE chromaticity coordinates x and y, dominant wavelength λ_D and excitation purity p_E, with Source C as the achromatic point.

2. Instruments

Three types of telephotometers were used. Two of them measure the spectral intensity distribution of the light entering the objective of the telephometer in the direction from the object to the instrument. The light is composed of the radiation which is reflected from the surface of the object and attenuated through the atmosphere it passes and the radiation scattered by floating particles in the air in the same direction. One of the instruments bases itself on the photoelectric spectroradiometric method and the other on the photographic method. The third one is a visual telephotometer by the Maxwellian view equipped with red, yellow and blue Lovibond Glasses set in the path of the comparison light. By an adequate combination of the three glasses the color of the comparison light can be made to match with the light from the object.

1) D. Nickerson, K.L. Kelly and K.F. Stultz: J. Opt. Soc. Am. 35, 297 (1945).
2) C.D. Hendley and S. Hecht: J. Opt. Soc. Am. 39, 870 (1949).
3) R. Penndorf: J. Opt. Soc. Am. 46, 180 (1956).
4) S.M. Newhall, D. Nickerson and D.B. Judd: J. Opt. Soc. Am. 33, 383 (1943).

Fig. 1 shows the appearance of the photoelectric telephotometer and Fig. 2 its schematic diagram. The light from the object, passing through the telescope unit, is focussed on the entrance slit of the monochromator. The comparison source, for which a 6 volts 6 watts exciter lamp is applied, is also focussed on the entrance slit. Mirrors 1′ and 2′ are placed above and below. Their surfaces are slightly inclined from the vertical in opposed directions so that the images of the object and the comparison source may be focussed at the same position of the entrance slit. Both beams are flickered by a sector disc rotated by a synchronous motor.

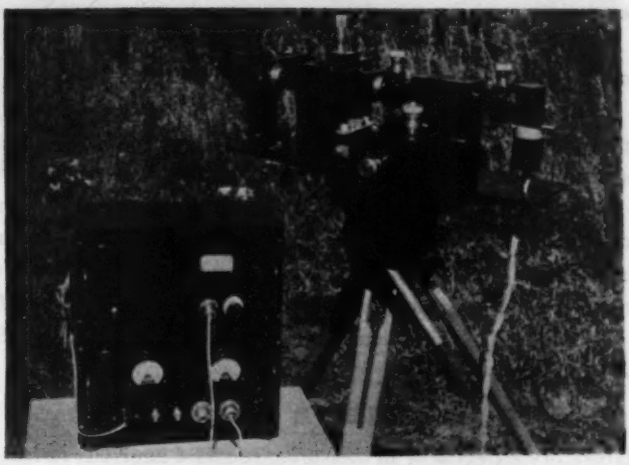

Fig. 1. The photoelectric telephotometer.

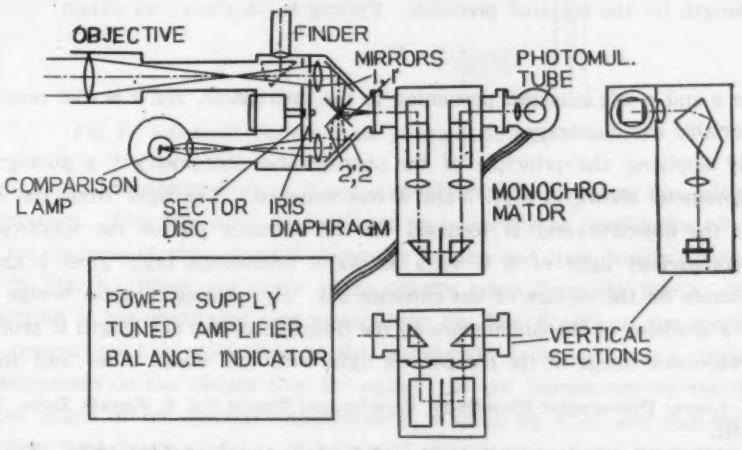

Fig. 2. Schematic diagram of the photoelectric telephotometer.

The variable iris diaphragm changes the ratio of the radiant flux of both beams. The monochromator, 120×275×175 mm, is specially designed for telephotometry. As shown in Fig. 2, two dispersion systems of the same structure are so arranged symmetrically to the central slit that they form a zero dispersion type double-monochromator. Wavelength of the exciting light is changed by rotating two dispersion prisms simultaneously around an axis. A photomultiplier tube 1P28 is used as a light detector. The alternating part of the photocurrent is amplified by a tuned amplifier of the flickering frequency. Its output circuit is connected to a microammeter which is used as a balance indicator. If the radiant fluxes of the two beams are not equal, the balance indicator shows deflection of considerable amount. By adjusting the dial attached to the variable diaphragm, the deflection can be minimized to make the two fluxes equal. The openings of the diaphragms are square-shaped and are so arranged that if the length of the side of the opening for the comparison light is r, that for the light from the object is given by $a-r$, where a is the length of the side of either of the squares when fully opened. The effective intensity of the light from the object entering the phototube at the wavelength λ is $b_{1,\lambda}\{(a-r)^2/a^2\}E_\lambda$, where E_λ gives the spectral energy distribution of the object light. For the comparison light, it is given by $b_{1,\lambda}'(r^2/a^2)E_{S_1,\lambda}$, where $E_{S_1,\lambda}$ gives the spectral intensity distribution of the comparison light. By equating them we obtain

$$E_\lambda=(b_{1,\lambda}/b_{1,\lambda}')\cdot\{r^2/(a-r)^2\}\cdot E_{S_1,\lambda}\ .$$

From the laboratory experiment in measuring standard luminous surfaces of known spectral distributions, $b_{1,\lambda}/b_{1,\lambda}'$ was ascertained to be a constant independent of the wavelength for the required precision. Putting $b_{1,\lambda}/b_{1,\lambda}'=c_1$, we obtain

$$E_\lambda=c_1\cdot\{r^2/(a-r)^2\}\cdot E_{S_1,\lambda}\ , \qquad (1)$$

where a and c_1 are constants pertaining to the instrument, and r is dial reading of the variable iris diaphragm.

By applying the principle of the photographic photometry[5,6] a photographic telephotometer shown in Figs. 3 and 4 was designed. The light from the object enters the objective and is focussed on the entrance slit of the spectrograph. The comparison light of a 6 volts 30 watts microscope lamp gives a uniform illuminance on the surface of the entrance slit. By placing a glass wedge filter there a gradient of the illuminance to the direction of the slit length is produced. The dispersion image of the comparison light with the wedge filter and that of

5) Z. Koana: Photographic Photometry, Experimental Physics Vol. 6, Kawade Shobo, Tokyo, 1941.

6) J.W.T. Walsh: Photometry, Constable and Co. Ltd., London, 2nd Ed. 1953.

Fig. 3. The photographic telephometer.

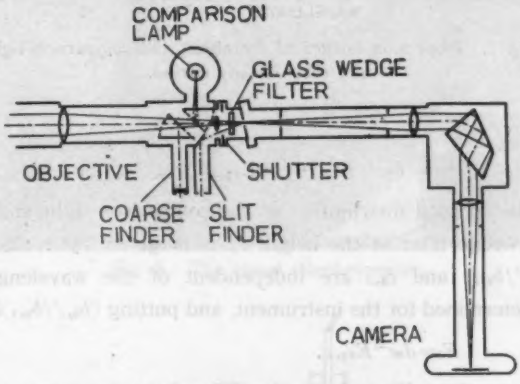

Fig. 4. Schematic diagram of the photographic telephotometer.

the light from the object without it are photographed on the same film with the same exposure. The film must be developed as uniformly as possible for all part of it. An example of photographed dispersion images and their density curves are shown in Fig. 5. When the curve of the density taken along the line **A**−**A′** on the spectrum of the object and that taken along the line **B**−**B′** on the spectrum of the comparison light intersects at the wavelength λ (lower figure), there the two illuminances on the camera film are equal. As the illuminance by the light from the object of the spectral distribution E_λ is given by $b_{3,\lambda}E_\lambda$ and that for the comparison light by $b_{3,\lambda}'\tau_\lambda E_{s_3,\lambda}$, the spectral distribution of the light from the

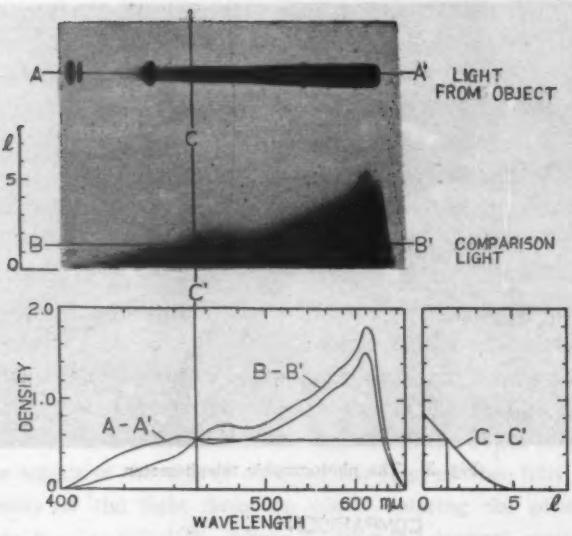

Fig. 5. Dispersion images of the object and comparison light, and their density curves.

object is given by

$$E_\lambda=(b_{2,\lambda}'/b_{2,\lambda})\cdot\tau_l\cdot E_{S_2,\lambda}$$

where $E_{S_2,\lambda}$ is the spectral distribution of the comparison light and τ_l is the transmittance of the wedge filter at the height l; τ_l is given by $\tau_l=c_{2,\lambda}e^{-l}$. Assuming again that $(b_{2,\lambda}'/b_{2,\lambda})$ and $c_{2,\lambda}$ are independent of the wavelength and are the constants to be determined for the instrument, and putting $(b_{2,\lambda}'/b_{2,\lambda})c_{2,\lambda}=d_2$, we have

$$E_\lambda=d_2e^{-l}E_{S_2,\lambda}. \qquad (2)$$

From E_λ in equations (1) and (2) the CIE tristimulus values are computed by

$$X=\int_{400}^{700}E_\lambda\bar{x}_\lambda d\lambda,\quad Y=\int_{400}^{700}E_\lambda\bar{y}_\lambda d\lambda,\quad Z=\int_{400}^{700}E_\lambda\bar{z}_\lambda d\lambda. \qquad (3)$$

By normalizing X, Y and Z, chromaticity coordinates x, y and z are obtained.

In both instruments, the opening angles are determined by the slit widths of monochromators. By the actual observation they were in most cases 0.5-0.7° horizontally and 0.7-1° vertically.

An old visual telephotometer by the Maxwellian view[7,8] was improved so that

7) S. Okamatsu: J. Illum. Eng. Inst. (Tokyo), 26, 435 (1942).
8) W.E.K. Middleton: Vision through the Atmosphere, Toronto Univ. Press, 1952.

three Lovibond glasses (red, yellow and blue) can be inserted in the path of the comparison light, for which the comparison source of a Macbeth illuminometer is used. Its appearance and schematic diagram are shown in Figs. 6 and 7. Images of the object and a pinhole at the diffusing glass of the comparison source are focussed at the artificial pupil of the instrument. Observing from the artificial pupil, one can see the surface of the lens as a uniform bright surface. By the Lummer-Brodhun cube, one half of the visual field corresponds to the light from the object and the other to the comparison light. By changing the intensity of the comparison light and the combination of three Lovibond glasses, luminances and colors of both

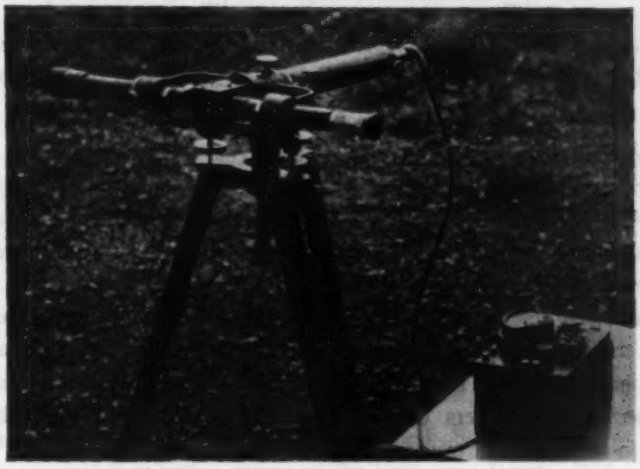

Fig. 6. The visual telephotometer.

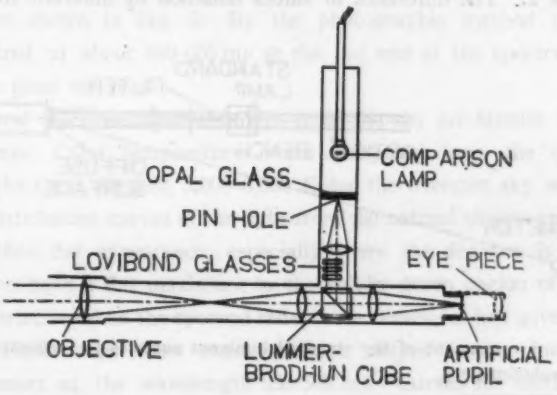

Fig. 7. Schematic diagram of the visual telephotometer.

the half visual fields are made to match. This is based on the principle of the subtractive color matching by which a fairly good accuracy is obtained, for in this case the spectral distribution of the comparison light resembles that of the light from the object[9]. The visual angle of this telephotometer is about 1° in diameter. The luminance of the lens by the light from the object is given by $B=\int_{400}^{700} b_{s,\lambda} E_\lambda \bar{y}_\lambda d\lambda$. As $b_{s,\lambda}$ can be regarded as independent of the wavelength in the required precision, by putting $b_{s,\lambda} \fallingdotseq b_s$ we have $B=\int_{400}^{700} E_\lambda \bar{y}_\lambda d\lambda \fallingdotseq b_s E$ where E is the apparent luminance of the object. The luminance by the comparison light is given by

$$B'=\int_{400}^{700} b_{s,\lambda}' E_{S_3,\lambda} \tau_{R,\lambda} \tau_{Y,\lambda} \tau_{B,\lambda} \bar{y}_\lambda d\lambda \fallingdotseq b_s' \int_{400}^{700} E_{S_3,\lambda} \tau_{R,\lambda} \tau_{Y,\lambda} \tau_{B,\lambda} \bar{y}_\lambda d\lambda ,$$

where $\tau_{R,\lambda}$, $\tau_{Y,\lambda}$ and $\tau_{B,\lambda}$ are respectively the spectral transmittances of the red, yellow and blue Lovibond glasses. By putting $B=B'$ and $b_s'/b_s=c_s$, the apparent luminance of the object becomes

$$E=c_s \int_{400}^{700} E_{S_3,\lambda} \tau_{R,\lambda} \tau_{Y,\lambda} \tau_{B,\lambda} y_\lambda d\lambda$$

and simultaneously tristimulus values are given by

$$X=c_s \int_{400}^{700} E_{S_3,\lambda} \tau_{R,\lambda} \tau_{Y,\lambda} \tau_{B,\lambda} \bar{x}_\lambda d\lambda , \quad \text{etc.} \qquad (4)$$

All the above mentioned instruments were calibrated in the laboratory by measuring the diffuse luminous surfaces of known luminances and spectral distributions arranged as shown in Fig. 8. To cover a wide range of luminance of natural objects, neutral filters were applied. As these neutral filters have some selectivity in their spectral transmittances, corrections had to be made.

The results of the experiment with which the instruments can be compared are shown in Table 1. The difference in values obtained by different instruments for

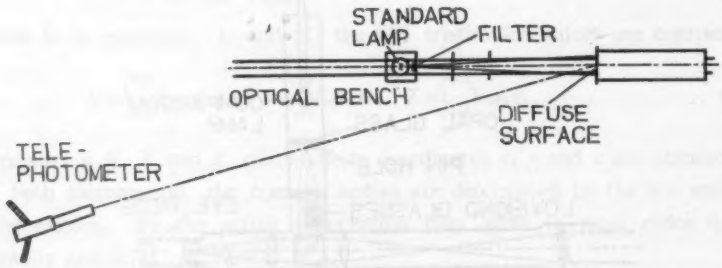

Fig. 8. Arrangement of the standard luminous surfaces for calibration of telephotometers.

9) D.B. Judd: Color in Business, Science and Industry, John Wiley and Sons Inc., N.Y., 1952.

Table 1. Comparion of the instruments.

Object	Distance (km)	Weather	x	y	λ_D (mμ)	p_E (%)	x	y	λ_D (mμ)	p_E (%)
			Photoelectric method				Visual method			
Forest	0.6	clear	0.337	0.373	568	22	0.333	0.367	568	20
Field crops	0	clear	0.364	0.436	567	47	0.363	0.432	568	45
Sky	—	overcast	0.308	0.325	540	2	0.310	0.335	550	5
Sky	—	clear	0.271	0.300	486	16	0.274	0.307	468	14
			Photographic method				Visual method			
Sky	—	clear	0.257	0.256	475	27	0.264	0.261	474	23
Sky	—	overcast	0.316	0.359	558	13	0.315	0.353	558	11
Building	0.4	overcast	0.363	0.392	573	35	0.366	0.395	573	36
Grass	0	overcast	0.362	0.401	571	36	0.358	0.395	571	34

the same object occurs not only from the instrumental errors but also from the fact that the measured area of objects is somewhat different by instruments as their viewing angles are not the same. These differences are, though they are a little larger than the errors expected by the ordinary color measurement in the laboratory, not considered to be important as the apparent colors of natural objects vary to a much larger extent by the weather or the measured area of the objects.

3. Experimental results

3.1 Spectral distributions of the light from natural objects

Typical spectral distribution curves of the light from forests, field crops, earth, grass, buildings and the sky near the horizon measured by the above-mentioned instruments are shown in Eig. 9. By the photographic method the measurable region is limited to about 640-660 mμ at the red end of the spectrum as ordinary pranchromatic films are used.

The spectral distribution of the light from the sky are similar to those in the previous reports. Color temperatures were computed from the curves; 10,000-20,000°K for the clear sky and 5,000-6,000°K for the overcast sky were obtained.

Spectral distribution curves of the light from the natural objects are characterized generally by their flat appearance, especially when the distance is large. Curves taken for forests have a flat maximum in the yellow green region of the spectrum; they are less selective than the spectral reflectance curves for leaf given by Nickerson and others. Field crops show most selective curves among measured objects with a maximum at the wavelength 550-570 mμ. Curves for earth and buildings go up slowly with increasing wavelength.

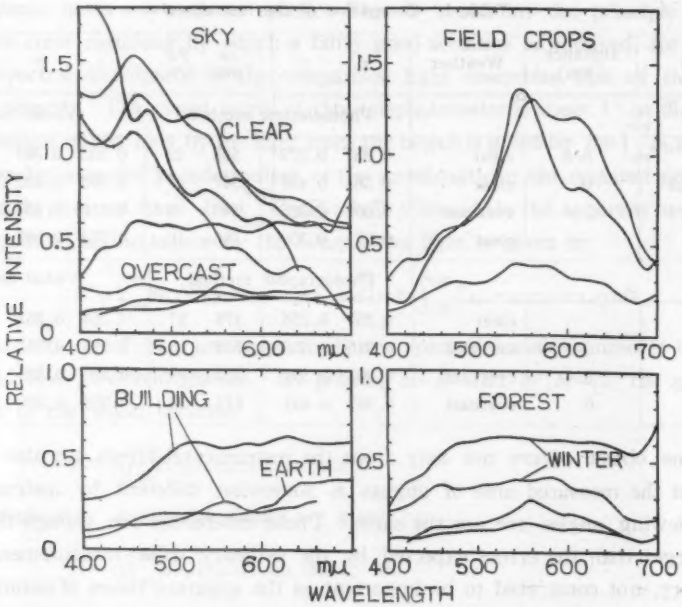

Fig. 9. Spectral distribution curves of the light from natural objects. Scales of spectral intensity are taken arbitrarily for various objects.

3.2 Apparent chromaticities of natural objects

Chromaticities of natural objects which were measured are shown in Table 2 and Figs. 10 and 11.

Table 2. Chromaticity of natural objects.

Object	Season	Weather	Distance (km)	x	y	λ_D (mμ)	p_E (%)
I. Foliage							
deciduous forest	spring	overcast	0	0.355	0.428	566	42
			0.1	0.339	0.383	567	26
				0.351	0.407	568	35
				0.360	0.419	568	41
				0.366	0.433	568	46
	autumn	clear	0	0.310	0.350	551	9
			0.1	0.317	0.359	558	13
coniferous forest	winter	overcast	0	0.315	0.375	555	17
				0.316	0.343	560	9
				0.347	0.424	564	39
				0.325	0.355	566	15
				0.330	0.365	566	18
				0.358	0.432	566	44
				0.356	0.411	568	38
				0.363	0.408	570	39

(*Continued*)

Object	Season	Weather	Distance (km)	x	y	λ_D (mμ)	p_E (%)
	spring	clear	0.25	0.348	0.423	565	39
				0.351	0.411	567	37
				0.341	0.383	568	26
				0.355	0.404	569	36
deciduous forest	spring	clear	0.25	0.333	0.409	561	31
				0.330	0.393	562	26
				0.333	0.407	562	30
				0.348	0.423	565	39
			0.7	0.333	0.376	566	22
				0.355	0.404	569	36
coniferous forest		overcast	0.25	0.281	0.307	487	12
				0.287	0.343	505	8
				0.310	0.346	550	8
				0.319	0.386	557	21
				0.318	0.356	560	13
				0.325	0.381	561	21
				0.331	0.391	563	26
				0.322	0.353	564	13
				0.325	0.357	565	15
deciduous forest	spring	overcast	0.25	0.291	0.346	512	7
			0.7	0.307	0.367	548	13
				0.311	0.331	553	4
				0.315	0.382	555	19
			0.25	0.319	0.386	557	21
				0.325	0.397	560	26
				0.337	0.376	567	23
				0.339	0.383	567	26
coniferous forest	summer	clear	0.6	0.313	0.345	556	8
				0.313	0.337	558	6
				0.314	0.339	559	7
				0.358	0.401	570	36
		overcast	0.6	0.289	0.322	494	7
				0.291	0.325	497	7
				0.308	0.338	545	5
				0.312	0.345	554	8
				0.317	0.361	558	14
				0.314	0.339	559	7
				0.329	0.384	563	23
				0.336	0.398	564	29
				0.342	0.413	564	35
				0.320	0.344	565	10
	autumn	clear	0.25	0.303	0.363	542	11
				0.303	0.379	544	15
				0.308	0.370	549	14
				0.318	0.393	556	23
				0.334	0.415	561	33
				0.339	0.411	563	33
				0.338	0.390	565	27
deciduous forest	autumn	clear	0.7	0.265	0.272	478	21
				0.279	0.311	489	12
				0.308	0.378	550	16
				0.310	0.352	551	10
			0.4	0.318	0.358	560	14
			0.2	0.323	0.368	562	17
			0.3	0.324	0.365	563	17
			0.7	0.338	0.381	567	25

(*Continued*)

Object	Season	Weather	Distance (km)	x	y	λ_D (mμ)	p_E (%)
coniferous forest	autumn	overcast	0.7	0.293	0.307	484	7
				0.287	0.303	484	10
				0.284	0.306	486	11
				0.292	0.312	488	7
				0.291	0.315	490	7
				0.311	0.375	552	16
				0.313	0.354	555	11
				0.314	0.362	556	14
				0.320	0.366	560	16
				0.329	0.368	565	19
				0.336	0.382	566	25
deciduous forest	autumn	overcast	0.7	0.310	0.360	551	12
				0.324	0.375	561	20
				0.363	0.388	574	34
coniferous forest	winter	clear	0.25	0.302	0.320	497	3
			0.6	0.315	0.337	561	7
				0.316	0.336	563	7
				0.331	0.345	573	13
			0.25	0.322	0.332	574	8
			0.6	0.336	0.348	575	15
				0.360	0.375	575	29
				0.346	0.353	577	19
				0.362	0.364	579	27
			0.25	0.353	0.349	582	20
deciduous forest			0.6	0.327	0.352	568	14
				0.351	0.350	580	20
				0.374	0.366	581	30
coniferous forest	spring	clear	2.7	0.307	0.363	548	12
				0.310	0.345	551	8
			2	0.310	0.353	551	10
			2.7	0.315	0.379	555	18
				0.333	0.376	566	22
				0.321	0.340	568	9
				0.332	0.362	568	18
		overcast	2.7	0.276	0.288	480	16
				0.281	0.303	485	12
				0.288	0.319	492	8
				0.305	0.330	525	3
				0.315	0.338	560	7
	autumn	clear	2	0.270	0.289	482	18
			2.7	0.264	0.283	482	20
				0.268	0.290	483	18
				0.275	0.298	484	15
				0.274	0.303	486	15
			2	0.280	0.310	488	12
			2.7	0.283	0.312	489	10
			2	0.291	0.335	504	6

(*Continued*)

Object	Season	Weather	Distance (km)	x	y	λ_D (mμ)	p_E (%)
coniferous forest	autumn	overcast	2.7	0.260	0.272	479	23
				0.288	0.302	483	10
				0.268	0.290	483	18
				0.289	0.308	486	9
			2	0.300	0.325	502	3
				0.300	0.330	509	3
deciduous forest	winter	clear	2	0.285	0.293	479	12
				0.296	0.323	497	5
		overcast	2	0.303	0.329	514	3
				0.317	0.356	559	13
				0.316	0.340	561	8
				0.343	0.388	568	28
				0.343	0.355	575	19
deciduous forest	spring	clear	6	0.293	0.310	486	7
				0.285	0.310	488	10
				0.291	0.323	495	7
				0.292	0.326	497	6
		overcast	6	0.288	0.295	478	10
				0.279	0.298	484	13
				0.299	0.318	493	4
	autumn	clear	6	0.270	0.274	477	20
				0.264	0.280	481	21
				0.268	0.291	483	18
				0.285	0.303	484	10
				0.285	0.304	485	10
				0.270	0.296	485	17
	winter	clear	6	0.268	0.275	478	20
				0.302	0.320	497	3
coniferous forest	spring	clear	8	0.280	0.291	480	14
				0.293	0.310	486	7
				0.285	0.310	488	10
				0.297	0.314	489	5
				0.287	0.314	490	9
		overcast	8	0.286	0.290	476	12
				0.258	0.274	480	24
				0.294	0.312	487	6
	autumn	clear	8	0.261	0.275	480	22
				0.269	0.286	482	18
				0.274	0.294	483	16
deciduous forest	spring	clear	9	0.284	0.292	479	12
				0.284	0.294	480	12
				0.295	0.306	482	7
				0.293	0.309	486	7
				0.287	0.314	490	9
				0.292	0.321	494	6
		overcast		0.292	0.309	486	7
		clear	16	0.284	0.292	479	12
				0.279	0.292	481	14
				0.295	0.309	485	6
				0.296	0.312	487	6
II. Bamboo-grove							
	winter	clear	0.6	0.344	0.360	574	21
				0.354	0.366	576	25

(*Continued*)

Object	Season	Weather	Distance (km)	x	y	λ_D (mμ)	p_E (%)
III. Grass							
green	autumn	clear	0.6	0.317	0.359	558	13
grass			0.25	0.330	0.397	562	27
				0.343	0.417	564	36
		overcast	0.25	0.336	0.348	575	15
dry grass	winter	clear	0.1	0.403	0.388	581	44
				0.405	0.390	581	45
				0.382	0.359	585	31
			6	0.299	0.322	497	4
IV. Field crops							
	summer	clear	0	0.336	0.409	563	32
				0.374	0.432	570	48
		overcast	0	0.330	0.402	561	29
				0.334	0.399	563	29
				0.351	0.424	566	40
				0.361	0.414	569	40
	autumn	clear	0	0.361	0.443	566	48
				0.357	0.416	568	39
		overcast	0	0.361	0.443	566	48
				0.372	0.449	568	52
	summer	clear	0.6	0.389	0.379	581	38
		overcast	0.6	0.330	0.402	561	29
				0.334	0.399	563	29
				0.337	0.397	564	29
				0.342	0.413	564	35
				0.358	0.401	570	36
	autumn	clear	0.6	0.329	0.379	563	22
				0.334	0.393	564	27
			0.3	0.354	0.413	568	38
		overcast	0.6	0.310	0.366	551	14
				0.323	0.387	559	23
V. Vegetables							
	summer	clear	0.6	0.328	0.361	566	17
				0.332	0.362	568	18
			0.3	0.350	0.400	568	33
			0.6	0.328	0.352	569	15
			0.3	0.349	0.394	569	31
			0.6	0.353	0.391	570	32
			0.3	0.374	0.432	570	48
		overcast	0.3	0.322	0.388	559	22
			0.6	0.325	0.367	563	18
				0.334	0.399	563	29
				0.342	0.413	514	35
				0.330	0.374	565	21
			0.3	0.351	0.424	566	40
VI. Building							
	spring	overcast	0.5	0.309	0.326	545	3
				0.316	0.343	560	9

(*Continued*)

Object	Season	Weather	Distance (km)	x	y	λ_D (mμ)	p_E (%)
	spring	overcast	0.5	0.316	0.340	561	8
				0.325	0.355	566	15
				0.345	0.375	571	25
				0.352	0.368	575	25
				0.360	0.364	578	26
			1	0.316	0.340	561	8
				0.312	0.322	566	2
				0.321	0.339	568	9
				0.352	0.368	575	25
				0.350	0.360	576	22
	winter	overcast	2	0.281	0.297	482	13
				0.301	0.317	491	3
				0.296	0.323	497	5
				0.303	0.329	514	3
				0.308	0.325	535	2
				0.312	0.345	554	8
				0.316	0.340	561	8
VII. Earth							
	winter	clear	0.6	0.349	0.351	579	20
				0.369	0.370	579	30
				0.371	0.367	580	30
		overcast	2	0.316	0.340	561	8
				0.315	0.329	565	5
				0.325	0.355	566	15
				0.322	0.335	571	8
				0.313	0.321	574	2
				0.389	0.364	585	34
	autumn	clear	9	0.273	0.282	479	17
				0.281	0.294	481	13
				0.275	0.297	484	15
				0.281	0.306	487	12
			16	0.257	0.268	479	25
VIII. Water (sea surface)							
	winter	overcast	0.3	0.281	0.297	482	13
				0.289	0.314	490	8
				0.301	0.319	495	3
				0.298	0.323	498	4
				0.303	0.329	514	3
				0.309	0.334	548	5
				0.312	0.345	554	8
	spring	overcast	1	0.316	0.340	561	8
	winter	overcast	1	0.266	0.279	480	20
				0.289	0.314	490	8
				0.296	0.323	497	5
				0.298	0.323	498	4
				0.303	0.329	514	3
				0.309	0.334	548	5
				0.312	0.349	554	9
				0.316	0.346	560	10
				0.316	0.340	561	8
IX. Snow surface							
	winter	clear	0.25	0.273	0.290	482	16

(*Continued*)

Object	Season	Weather	Distance (km)	x	y	λ_D (mμ)	p_E (%)
				0.300	0.329	508	3
				0.311	0.341	552	7
				0.317	0.348	560	10
				0.323	0.343	568	11
			2.7	0.313	0.339	558	7
				0.315	0.338	560	7
				0.317	0.336	565	7
			8	0.315	0.338	560	7
				0.320	0.357	561	14
				0.319	0.347	563	11
				0.323	0.343	568	11
			9	0.316	0.337	563	7
				0.323	0.343	568	11
			16	0.279	0.292	481	14
				0.300	0.325	502	3
				0.308	0.344	547	7
				0.317	0.348	560	10
				0.316	0.337	563	7
				0.315	0.338	560	7
				0.320	0.346	564	11
X. Sky near the horizon							
	spring	overcast		0.316	0.340	561	8
				0.343	0.355	575	19
				0.363	0.375	576	30
	autumn	overcast		0.299	0.325	500	4
				0.305	0.343	540	6
				0.315	0.337	561	7
				0.317	0.335	565	7
	winter	clear		0.254	0.263	478	26
				0.268	0.282	480	19
				0.279	0.292	481	14
				0.284	0.304	484	11
				0.293	0.310	486	7
				0.271	0.300	486	16
				0.288	0.310	487	9
				0.269	0.319	492	15
		overcast		0.292	0.330	500	6
				0.303	0.329	514	3
				0.308	0.325	535	2
				0.309	0.330	546	4
				0.309	0.334	548	5
				0.311	0.341	552	7
				0.312	0.332	557	5
				0.317	0.350	560	11
				0.315	0.338	560	7
				0.323	0.356	564	14
				0.321	0.333	572	8
				0.332	0.348	572	15
				0.340	0.345	578	16
				0.348	0.349	580	19
				0.351	0.350	580	20

Foliage at a distance less than 1 kilometer are yellow-green of dominant wavelength 542-582 mμ except on a heavily overcast hazy day when unsaturated blue was observed. The maximum excitation purity is 49% for leaves in the

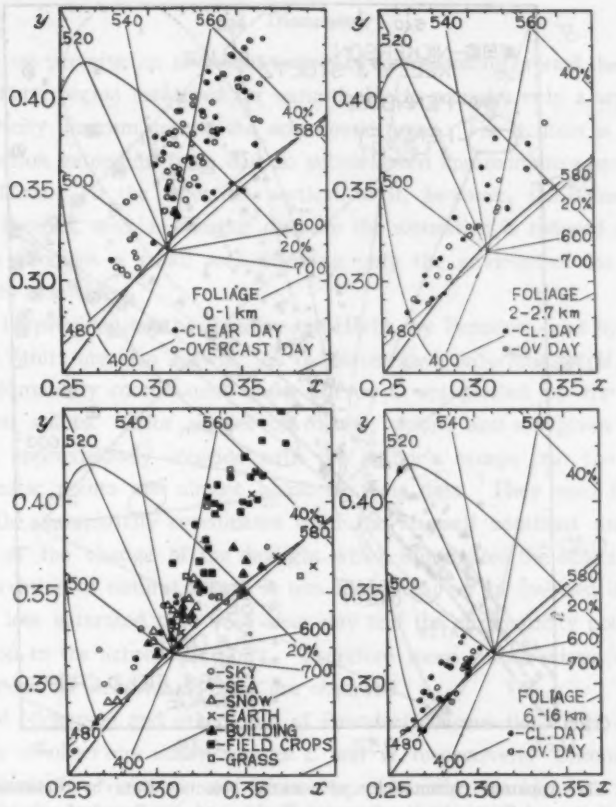

Fig. 10. Apparent chromaticity of natural objects.

vicinity of the instrument. In winter they appear more yellowish. Though the apparent luminance of the deciduous forests is generally higher than that of the coniferous forests, no essential difference in their chromaticity was observed except in winter. At distances 2-2.7 kilometers foliage cover the color region from yellow-green to blue. The maximum excitation purity is 28% for yellow-green side. At a distance more than 6 kilometers apparent colors of forests are blue or blue-green of dominant wavelength 470-497 mμ and the maximum excitation purity 24%.

Green grasses in the vicinity of the instrument appear as yellow-green of dominant wavelength 558-564 mμ and the maximum excitation purity 36%. Dry grasses are yellow of dominant wavelength 575-585 mμ and the maximum excitation

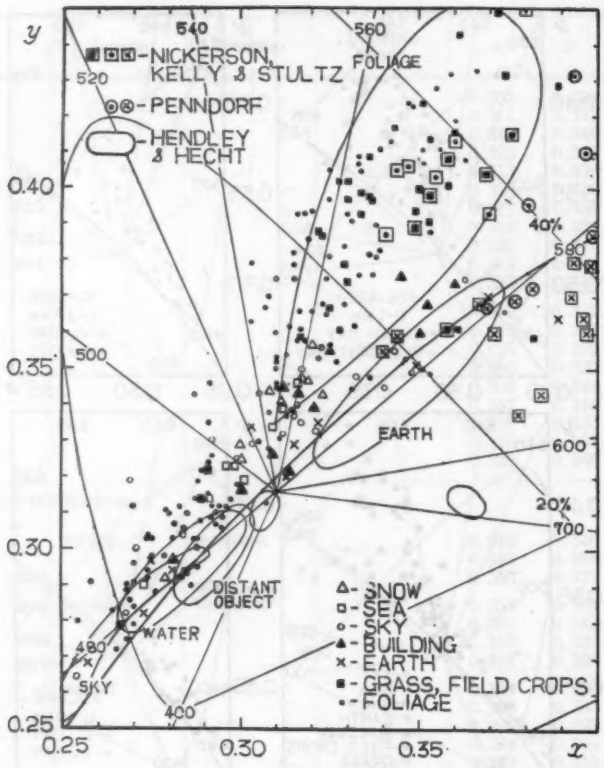

Fig. 11. Apparent chromaticity of natural objects. Data by Nickerson, Kelly and Stultz, by Hendley and Hecht, and by Penndorf are also shown.

purity 45%. Field crops and vegetables show most saturated colors among the measured objects. They are yellow-green of dominant wavelength 561-570 mμ and the maximum excitation purity 52%.

Earth at a distance less than 2 kilometers appears yellow of dominant wavelength 561-585 mμ and the maximum excitation purity 36%. Buildings appear in general as unsaturated yellow or grey with maximum excitation purity of 26%.

Sea surfaces were measured only on overcast days. Their chromaticity points are distributed around the achromatic point. Maximum excitation purity is 10% for yellow-green and 20% for blue. Chromaticity points for snow surfaces and for overcast sky are also distributed around it. The clear sky is blue of dominant wavelength 478-492 mμ with the maximum excitation purity 26%.

4. Discussion

Though we perceive an abundant variety of colors looking around the landscape, the chromaticity region measured for natural objects occupies only a small part of the chromaticity diagram around the achromatic point. The domain is fairly wide for the direction extending from blue to yellow-green approximately parallel to the blackbody locus. To the direction vertical to it, however, the domain is much narrower. Besides, with increasing distance the saturation is reduced quickly and the domain becomes a small area covering only the environs of the achromatic point and its blue side.

In Fig. 11, previous data by Hendley and Hecht, by Penndorf, and by Nickerson, Kelley and Stultz are also shown. As the latter gave only Munsell H, V, and C, the CIE chromaticity coordinantes under Source C are plotted by the author for their typical values. Color ranges of foliage, water, and sky given by Hendley and Hecht approximately coincide with the author's except that the environs of the achromatic points are almost blank in their data. They used Source C for obtaining the chromaticity coordinates from the Munsell notations and neglected the effect of the change of the daylight which illuminates the object. From the direct observation of natural objects it was found that on an overcast day apparent colors are less saturated than on a clear day and the chromaticity points move in the direction to the achromatic point. Therefore more colors whose chromaticity points lie near the achromatic point are observed.

Data of Nickerson and others and of Penndorf concern the colors of objects in the vicinity of observers under Sources C and B respectively. Chromaticities for leaf and grass by Nickerson and others approximately coincide with those by the author but by Penndorf they are more yellowish green.

As already mentioned, the reflected light from the surfaces of natural objects attenuates through the atmosphere and the airlight scattered by the particle in the path toward the instrument is added to it. Therefore the spectral distribution of the light incident to the instrument is less selective than the initial reflected light and the apparent color of the objects becomes less saturated or their chromaticity point moves in the direction to blue. This is shown from the data given in Table 2 and Fig. 10. Middleton[10] treated this problem theoretically and calculated the change of colors with distance. Fig. 12 shows the average values of the chromaticity coordinates measured for foliage at various distances in spring and the calculated result by Middleton for the typical grass color ($x=0.333$, $y=0.378$) in a light haze of the extinction coefficient $\sigma=0.0080\,\lambda^{-2.09}\,\mathrm{km}^{-1}$. There C_W is the

10) W.E.K. Middleton: J. Opt. Soc. Am. 40, 373 (1950).

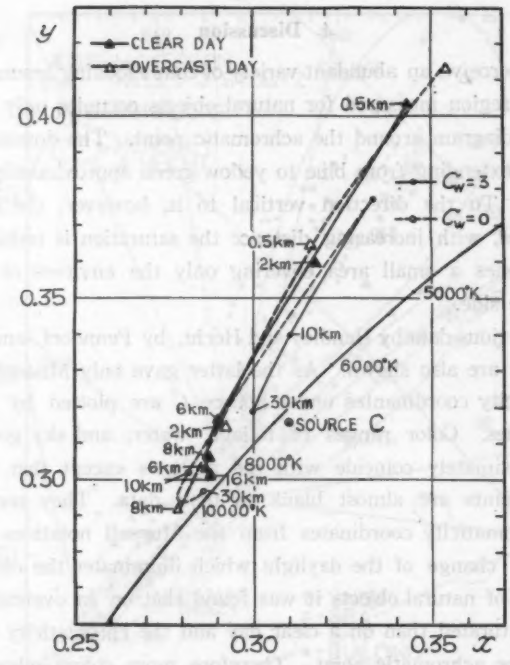

Fig. 12. Change of apparent chromaticity of foliage. Data computed by Middleton for typical grass color in a light haze are also shown.

contrast of the luminance between the ideal white surface near the observer and the sky near the horizon. The curve marked with $C_W=0$ represent the change of color on a perfectly overcast day and $C_W=3$ on a very clear day. It may be inadequate to compare directly the experimental and theoretical results, as the initial colors, C_W, and the extinction coefficients might differ in both cases, but it would seem that on an overcast day the experimental result coincides fairly well with the calculation. On a clear day, measured change of color seems to be greater than calculated.

5. Acknowledgement

The author extends his sincere gratitude to Prof. Y. Uchida of the Kyoto University, who gave important instructions to complete this work, and to Mr. H. Tanaka for his assistance in the experimental work.

Electrical Properties of Dielectric Films and Sensitivity of Dielectric Bolometer

I. The Effects of Temperature and Moisture Content

Tairi YAMASHITA

Faculty of Education, Kumamoto University

Abstract

Thermal changes of electrical resistance and capacity of humidified cellophane film are measured at temperatures between 10 and 85°C and at 60 and 1000 c/s. The measurement showed that the influence of moisture in the film on both resistance and capacity is remarkable, the influence being different above and below the temperature lying between 40 and 50°C. These observed results are discussed.

Introduction

P. Moon[1] and J. Ewles[2] showed that dielectric bolometers have higher sensitivity than metallic ones. The author, using films of various dielectric materials, designed and constructed bolometers[3][4]. The thermal influence on electrical resistance of the films at d.c. and a.c. 60 c/s was examined[5], and the circuit of bolometer bridge provided with thermal negative feed back was studied[6]. In spite of good stability of this bridge circuit, electrical characteristics of the film varied in air. As the irregurality seemed due to the change of moisture content of the dielectric film left exposed to air, the electrical resistance and capacity and dielectric loss of the film with various moisture content were measured, and from these measurement it became clear that moisture contained in the film has a serious effect on the electrical characteristics of bolometer.

Experimental

The principal apparatus used is illustrated in Fig. 1. A thin dielectric film S is sandwitched between two ebonite plates Ps with a hole of 6.75 cm^2 in area in

1) P. Moon & L.R. Steinhardt, J.O.S.A. **28** (1936) 148.
2) J. Ewles, J. Sci. Inst. **24** (1947) 57.
3) T. Yamashita, J. Phys. Soc. Jap., **5** (1950) 93.
4) T. Yamashita, Science of Light, **1** (1951) 51.
5) T. Yamashita, Memoirs Fac. Educ., Kumamoto Univ. **4** (1956) 138.
6) T. Yamashita, Memoirs Fac. Educ., Kumamoto Univ. **5** (1957) 185.

the center dividing a mercury-filled glass container G into two separate compartments, the mercury on both sides of the film serving as electrodes for the measurements to be made in the direction of thickness of the film at the mean of temperature read on two thermometers Ts inserted into the mercury electrodes.

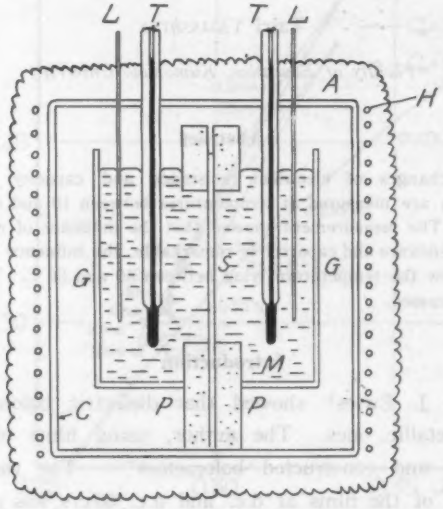

Fig. 1. Arrangement of apparatus.
A: asbestus, S: film, G: glass container, M: mercury, C: copper cylinder, P: ebonite plate, H: heater, L: lead wire, T: thermometer.

The above apparatus is placed in a copper cylindrical vessel C covered with a layer of asbestos A embedded with a heating resistance wire H. The measurement was carried out by applying low a.c. voltage at the frequencies of 60 c/s with OB-1 oscillator and 1000 c/s with an assembled tuning fork oscillator. To facillitate the

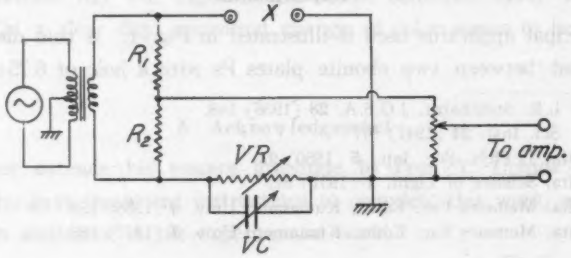

Fig. 2. The bridge.

measurement, a bridge circuit shown in Fig. 2 was used; its measurable ranges were 0~100 MΩ for resistance and 0~1 μF for capacity with the fixed ratio R_1/R_2= 1/1 of the bridge resistances. The circuit was calibrated by using standard resistors and standard capacitors.

The readings of *VR* and *VC* of the bridge give directly the values of electric resistance and capacity of the specimen within the error of 1%.

A 4:1 transformer was used to operate the bridge. As about 2V was applied to the primary of the transformer, the balancing arm voltages of the bridge were about 0.25 V each. A test on the stability of the bridge showed that even with the application of 50 V to the primary of the transformer, the reading became steady after 20 minutes from switching-on.

The output voltage of the bridge was observed with C.R.O. after being amplified by a narrow band width amplifier. Schematic diagram of the whole circuit is shown in Fig. 3.

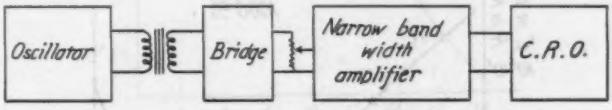

Fig. 3. Block diagram of the circuit for measurement

The control of the moisture content of the film is made as follows. The mercury in the electrode assemblage shown in Fig. 1 is emptied and the assemblage is supported upside down in a glass cylindrical vessel with H_2SO_4 solution at the

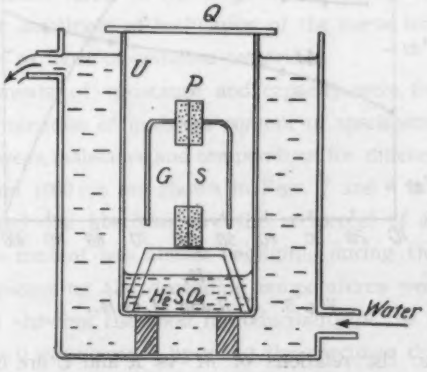

Fig. 4. Apparatus to measure *R*, *C*—*M* relation. P: ebonite plates, S: film, G: glass container supported upside down, U: glass cylinderical vessel, Q: glass plate

bottom, then the vessel is closed tightly at the top (see Fig. 4). The humidity in the vessel is controlled by the concentration of H_2SO_4 solution. The cylinder is left immersed in a water tank with running water for a whole day which sufficed for the film to become fully saturated with the given humidity at the temperature of the water. The electrode assembly is then taken out and dried mercury is quickly poured into it. When the intended measurements are over, the film is removed and weighed at once. The moisture content M is calculated from dehydrated weight.

The cellophane film used was 24.3 μ in thickness.

Results and considerations

The relation of relative humidity H_r vs electric resistance R and capacity C at 20°C and 1000 c/s and moisture content M are illustrated in Fig. 5.

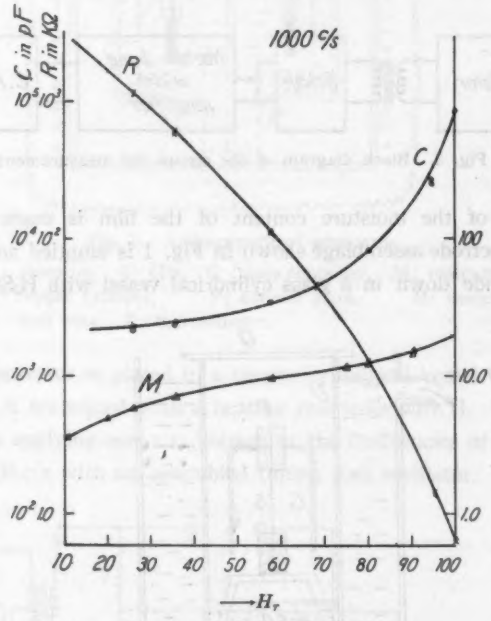

Fig. 5. C, R and M *vs* H_r.

From these data, the relations of M vs R and C are obtained as shown in Fig. 6.

R decreases very rapidly with increasing M or H_r. The variation of C is slow in comparison with R, especially when M or H_r is small.

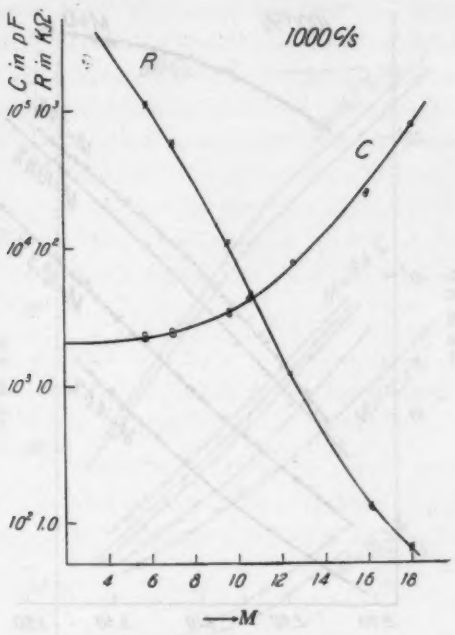

Fig. 6. *C*, *R* vs *M*.

As reported by Hearle[7] concerning other cellulose materials, the relation of log R to M is also almost linear in the neighborhood of $M=10\%$, in the case of cellophane film. The smallness of inclination of the curve for large M and small M is also in common to most of cellulose materials.

As the measurements of resistance and capacity were found perfectly reproducible, correct determination of moisture content of specimens was possible.

The relations between resistance and temperature for different moisture contents measured at 60 c/s and 1000 c/s are shown in Figs. 7 and 8 in which the ordinates are the resistance and the abscissas are the reciprocal of absolute temperature. Variation of moisture content was almost negligible during the measurement and observed values in ascending and decending temperatures were plotted at random to draw these curves showing the good reproducibility of the measurement.

The curve for $M=0$ was obtained by using the specimen dried at a temperature above 100°C. The variation of resistance with temperature is small when $M=0$, but when moist, it becomes noticeable. The temperature coefficient of resistance

7) J.W.S. Hearle: J. Text Inst. **44** (1953) T 117.

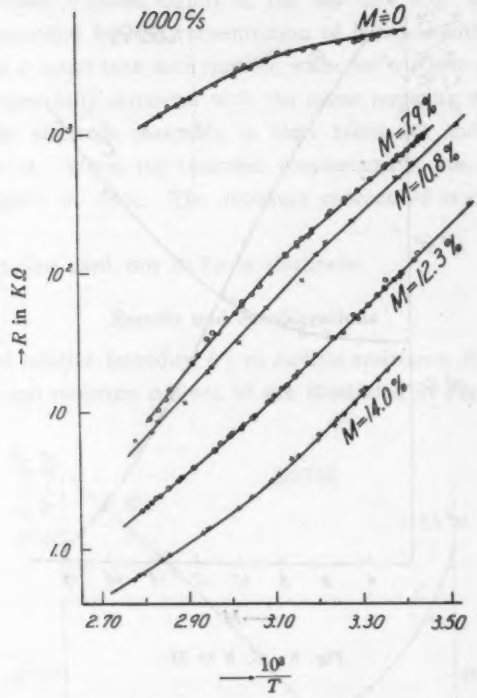

Fig. 7. R vs $\frac{1}{T}$.

is always negative. The absolute value of resistance decreases rapidly with increasing moisture content.

Every curve in these figures can be divided into two almost linear parts at 40~50°C. Hence the relation can be expressed as

$$\log R=\log R_0+E/kT \tag{1}$$

or

$$R=R_0 \exp (E/kT) \tag{2}$$

where E is the activation energy, k the Boltzmann constant and R_0 a constant.

From (1), the temperature coefficient α_r of resistance becomes

$$\alpha_r=\frac{1}{R}\frac{\partial R}{\partial T}=\frac{\partial \log R}{\partial T}=-\frac{E}{kT^2}<0 \tag{3}$$

Experimental data on E_1, E_2, E_2/E_1 and α_r at 20°C are listed in Tables 1 and

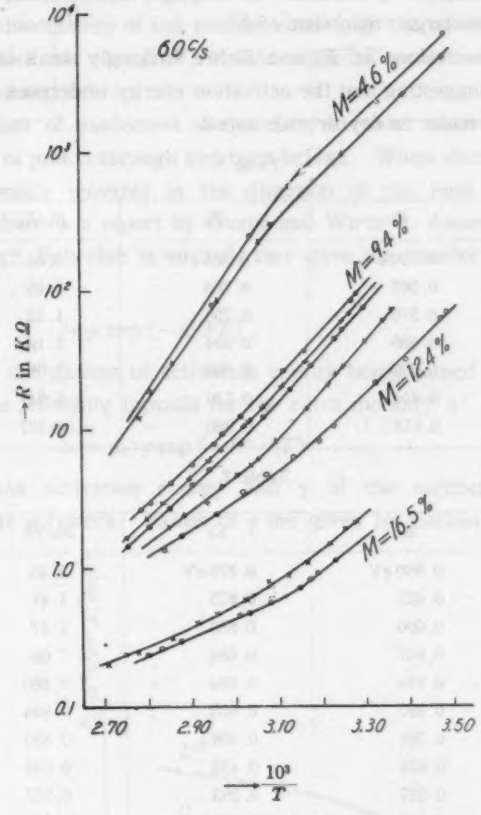

Fig. 8. R *vs* $\frac{1}{T}$.

2. E_1 is the value of E for the lower temperature side and E_2 for the higher temperature side of the curve. As seen from the tables, E_1 is only slighly influenced by the moisture content M but is inclined to decrease in the case of 60 c/s when M becomes large, so is also the temperature coefficient α_r at 20°C.

On the other hand, E_2, which remains almost unaltered while M is small, begins to decrease noticeably at $M=8\sim10\%$. It is $E_1<E_2$ when M is small, but as M increases, the relation between the two becomes $E_1=E_2$ then $E_1<E_2$ in both cases of 60 c/s and 1000 c/s.

The values of the temperature coefficient α_r given in the tables are over 10 times larger than α_r of Ni which is the largest among metals. Even in dry condi-

tion of $M=0$, in which α_r is reduced to about 1/4 of wet value, the coefficient is still about 2.5 times larger than that of Ni.

When dry, the values of E_1 and E_2 are strikingly small in comparison with those when moist suggesting that the activation energy undergoes an abrupt change in transition from moist to dry or vice versa.

Table 1.

(1000 c/s)

M	E_1	E_2	E_2/E_1	$-\alpha_r$
0.0%	0.120 eV	0.365 eV	3.04	0.0168
7.3	0.567	0.768	1.35	0.0795
7.9	0.570	0.750	1.33	0.0798
9.7	0.600	0.694	1.16	0.0840
10.8	0.605	0.660	1.09	0.0847
12.3	0.614	0.520	0.847	0.0858
14.0	0.618	0.386	0.627	0.0862

Table 2.

(60 c/s)

M	E_1	E_2	E_2/E_1	$-\alpha_r$
4.6%	0.600 eV	0.870 eV	1.45	0.0840
5.0	0.621	0.875	1.41	0.0870
5.2	0.600	0.880	1.47	0.0840
9.4	0.647	0.686	1.05	0.0907
10.0	0.710	0.624	0.880	0.0993
10.2	0.697	0.623	0.894	0.0975
10.4	0.701	0.594	0.850	0.0980
10.4	0.624	0.433	0.694	0.0873
15.5	0.527	0.293	0.557	0.0740
16.5	0.487	0.258	0.530	0.0681

Let us go into the cause of change of resistance due to miosture content and temperature. It is natural to consider that the conduction of electricity when dry is by cellophane itself and impurities contained in it, the mechanism of which is the same as in ordinary solid semi-conductors. In fact, the appearance of the curve resembles to that of solid semi-conductors containing impurities. When nearly dry, the water in cellophane is in the state of "bound water", but when very wet, almost all of the water is free water.

O'Sullivan[8] assumed that the capillary paths necessary for conduction are formed by such free water, the difference in water content being the difference in number of such paths and number of "breaks" within the paths affecting the

8) J.B. O'Sullivan: J. Text Inst. **39** (1948) T 368.

resistance, and also that the number of ions that participate in the conduction increases by the dissociation of ion sources caused by the existence of such water. Succeeding the idea of "breaks", Hearle regarded protons as the carriers of electricity in cellulose.

The mechanism of conduction of electricity in water caused by proton in this case is the jump of proton through hydrogen bridge. When electric field is applied, proton become easily movable in the direction of the field. As regards such extra mobolity, there is a report by Gierer and Wirtz[9]. Assuming that the jump of proton through H-bridge is normal, they gave the number of jump j per unit time as

$$j=j_0 \exp(-E/kT) , \qquad (4)$$

and considering the change of activation energy being caused by electric field F, they obtained the following formula for the extra mobility $u^{\pm}$

$$u^{\pm}=u_0^{\pm}\gamma \exp(-E^{\pm}/kT) \qquad (5)$$

where $E^{\pm}$ is the activation energy and γ is the number of H-bridge per molecule in linear polymers. Values of γ are given by Eucken; the curve of γ vs

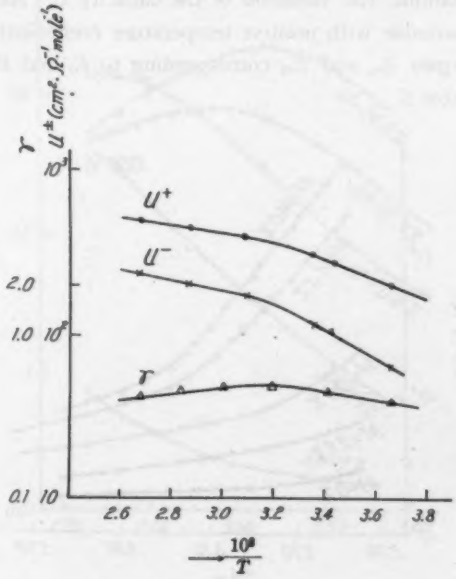

Fig. 9. $u^{\pm}$, γ vs $\frac{1}{T}$.

9) A. Gierer and K. Wirtz: J. Phys. Chem. **56** (1952) 914.

$1/T$ has a maximum at 40~50°C as shown in Fig. 9. It is remarkable that the number of broken hydrogen bridge is large at all temperatures.

$u^{\pm}$ depends on several parameters especially on temperature through γ as well as $\exp(-E^{\pm}/kT)$ as intermediary, the dependence being clearly seen in Fig. 9.

The electric conductivity σ is given by

$$\sigma = enu^{\pm}$$
$$= enu_0^{\pm}\gamma \exp(-E^{\pm}/kT) \qquad (6)$$

where e is the charge on an ion and n the number of ions in unit volume.

Hence, the resistance is given as

$$R = \frac{Kd}{enu_0^{\pm}\gamma S} \exp(E^{\pm}/kT) \qquad (7)$$

where d is the thickness of the specimen, S its area and K a constant. As γ undergoes no conspicuous change in the temperature range used in the experiment, the linear relation between $\log R$ and $1/T$ is well explained by (7). $1/\gamma$ has a minimum at 40~50°C which can be regarded as the cause of the change $E_1 < E_2 \rightarrow E_1 = E_2 \rightarrow E_1 > E_2$ by the increase of moisture content.

Let us next examine the variation of the capacity C. As shown in Fig. 10, the variation is remarkable with positive temperature coeffecient when very moist. The activation energies E_{c_1} and E_{c_2} corresponding to E_1 and E_2 were caulculated and are given in Table 3.

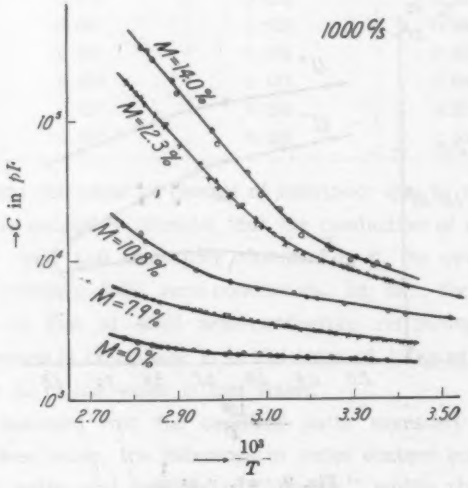

Fig. 10. C *vs* $\frac{1}{T}$.

Table 3.

(1000 c/s)

M	E_{c_1}	E_{c_2}	E_{c_2}/E_{c_1}	α_c
0.4%	0.0327 eV	0.0412 eV	1.25	0.00457
7.3	0.0785	0.0993	1.26	0.0110
7.9	0.0890	0.1200	1.34	0.0124
10.8	0.0970	0.334	3.44	0.0136
12.3	0.186	0.647	3.47	0.0260
14.0	0.202	0.770	3.81	0.0283

When not very miost, both E_{c_1} and E_{c_2} are about 1/10 of E_1 and E_2; they increase with the moisture ontent, E_{c_2} in particular, which increase rapidly at about $M=10\%$ at which the ratio E_{c_2}/E_{c_1} also becomes large. Above about $M=10\%$, E_{c_2} becomes larger than E_2 while E_{c_1} still remains smaller than E_1. Hence the temperature coefficient of resistance is manyfold larger than that of capacity at room temperature.

Lastly, $\tan\delta$ varies almost linearly with temperature when moisture content is

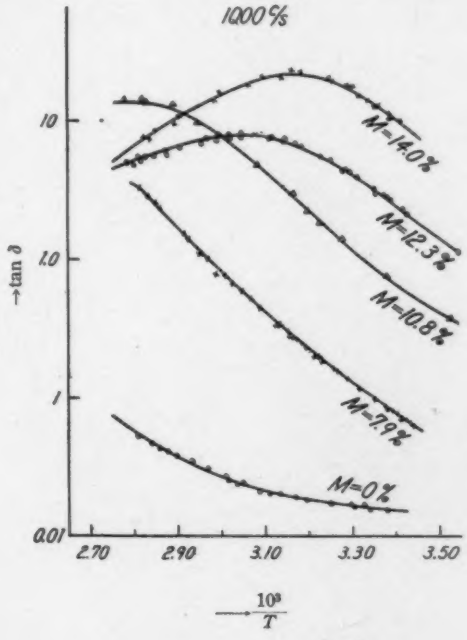

Fig. 11. $\tan\delta$ *vs* $\frac{1}{T}$

small, but as the latter increases, there appears a maximum on high temperature side shifting toward low temperature side as the moisture content further increases.

Temperature depenencies of capacity and tan δ similar to those observed at 1000 c/s are expected to appear at 60 c/s, for, up to about $M=5\%$, variations of resistance, capacity and tan δ at 1000 c/s and 60 c/s are of similar trend. But when the moisture content increases and with it the resistance drops very low, accurate measurement of capacity at 60 c/s becomes beyond the scope of the present experimental arrangement; for very high miosture content, detailed data were not obtained.

Acknowledgement

The auther wishes to express his sincere thanks to Dr. Y. Fujioka for his guidance and continued encouragement, to Prof. H. Ootuka, Director of the Institute for Optical Research, for his deep interest, to Prof. M Toda of Tokyo University of Education, Dr. K. Kudo, Dr. Y. Sakayanagi and other members of the Institute, for their valuable suggestions and discussions.

CONTENTS

Theory on Concave Grating Mountings for Photoelectric-Spectrometric Use
..... K. P. MIYAKE 39

Absorption Studies of Metastable Mercury Atoms in Argon-Mercury Discharge Afterglows ..... M. YOKOYAMA 59

Apparent Colors of Natural Objects ..... H. MASAKI 67

Electrical Properties of Dielectric Films and Sensitivity of Dielectric Bolometer.
(I) The Effects of Temperature and Moisture Content ..... T. YAMASHITA 87